High-Resolution Imaging of the M_L 2.9 August 2019 Earthquake in Lancashire, United Kingdom, Induced by Hydraulic Fracturing during Preston New Road PNR-2 Operations

Tom Kettley[*1,2], James P. Verdon[2], Antony Butcher[2], Matthew Hampson[3], and Lucy Craddock[3]

Abstract

Hydraulic fracturing (HF) at Preston New Road (PNR), Lancashire, United Kingdom, in August 2019, induced a number of felt earthquakes. The largest event (M_L 2.9) occurred on 26 August 2019, approximately three days after HF operations at the site had stopped. Following this, in November 2019, the United Kingdom Government announced a moratorium on HF for shale gas in England. Here we provide an analysis of the microseismic observations made during this case of HF-induced fault activation. More than 55,000 microseismic events were detected during operations using a downhole array, the vast majority measuring less than M_w 0. Event locations revealed the growth of hydraulic fractures and their interaction with several preexisting structures. The spatiotemporal distribution of events suggests that a hydraulic pathway was created between the injection points and a nearby northwest–southeast-striking fault, on which the largest events occurred. The aftershocks of the M_L 2.9 event clearly delineate the rupture plane, with their spatial distribution forming a halo of activity around the mainshock rupture area. Across clusters of events, the magnitude distributions are distinctly bimodal, with a lower Gutenberg–Richter *b*-value for events above M_w 0, suggesting a break in scaling between events associated with hydraulic fracture propagation, and events associated with activation of the fault. This poses a challenge for mitigation strategies that rely on extrapolating microseismicity observed during injection to forecast future behavior. The activated fault was well oriented for failure in the regional stress field, significantly more so than the fault activated during previous operations at PNR in 2018. The differing orientations within the stress field likely explain why this PNR-2 fault produced larger events compared with the 2018 sequence, despite receiving a smaller volume of injected fluid. This indicates that fault orientation and in situ stress conditions play a key role in controlling the severity of seismicity induced by HF.

Cite this article as Kettley, T., J. P. Verdon, A. Butcher, M. Hampson, and L. Craddock (2020). High-Resolution Imaging of the M_L 2.9 August 2019 Earthquake in Lancashire, United Kingdom, Induced by Hydraulic Fracturing during Preston New Road PNR-2 Operations, *Seismol. Res. Lett.* **92**, 151–169, doi: 10.1785/0220200187.

Supplemental Material

Introduction

Earthquakes caused by subsurface fluid injection have been widely reported globally and are associated with various industries, including geothermal energy (Deichmann and Giardini, 2009; Grigoli *et al.*, 2018; Kim *et al.*, 2018), underground wastewater disposal (Keranen *et al.*, 2013), and CO_2 sequestration (Stork *et al.*, 2015). For many years, hydraulic fracturing (HF) of low-permeability reservoirs was assumed to pose a relatively low risk of felt-induced seismicity, with the National Research Council (2012) suggesting that "the process of hydraulic fracturing… does not pose a high risk for induced felt seismic events (seismic magnitude M > 2)." Since then, however, HF-induced seismicity (HF-IS) has been observed in the United States (Holland, 2013; Skoumal *et al.*, 2018, 2019; Fasola *et al.*, 2019), the Western Canadian Sedimentary Basin (WCSB) (Schultz *et al.*, 2015; Bao and Eaton, 2016; Kao *et al.*, 2018; Roth *et al.*, 2020), and the Sichuan basin, China (Lei *et al.*, 2017; Meng *et al.*, 2019). Overall, cases of HF-IS are rare when compared with the total

1. Department of Earth Sciences, University of Oxford, Oxford, United Kingdom; 2. School of Earth Sciences, University of Bristol, Bristol, United Kingdom; 3. Cuadrilla Resources Ltd., Lancashire, United Kingdom

*Corresponding author: tom.kettley@earth.ox.ac.uk

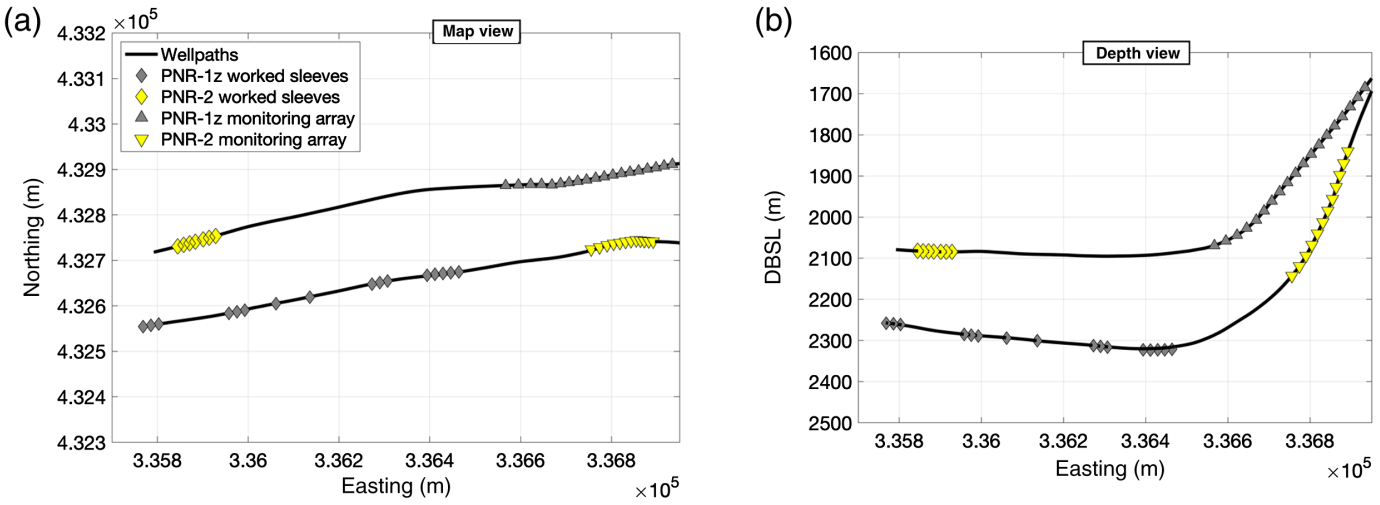

Figure 1. (a) Map and (b) depth view of the well paths and sliding sleeve locations worked during hydraulic fracturing at Preston New Road in 2018 (PNR-1z) and 2019 (PNR-2). Sleeves (shown as diamonds) are numbered from the toe (the further extent) to the heel of the well. Microseismic monitoring stations are shown as triangles. During PNR-2 operations in 2019, only the first seven sleeves were stimulated. The northing and easting here use the Ordnance Survey United Kingdom grid system, which continues throughout. The color version of this figure is available only in the electronic edition.

number of stimulated wells drilled, for example, Atkinson *et al.* (2016) showed that, even in one of the more seismically active basins (the WCSB), less than 1% of stimulated wells are associated with M > 3 events. The occurrence of HF-IS is extremely variable between different basins (e.g., Verdon *et al.*, 2016; van der Baan and Calixto, 2017) and even between different formations within the same basin (Skoumal *et al.*, 2018).

In the United Kingdom, only three wells have been hydraulically fractured within the Carboniferous Bowland Shale formation, and all have resulted in events of sufficient size to be felt by nearby populations. These wells lie within a few kilometers of each other on the Fylde Peninsula in Lancashire, northwest England, and were operated by Cuadrilla Resources Ltd. (CRL). The first of these was the Preese Hall well, which was stimulated in 2011, producing a local magnitude M_L 2.3 event on a northeast–southwest trending fault that was visible in reflection seismic data acquired post-injection in 2012 (Clarke *et al.*, 2014). This led to the imposition of a moratorium for over a year by the government, after which a traffic light scheme (TLS) was introduced to mitigate induced seismicity at future sites (Green *et al.*, 2012; Oil and Gas Authority, 2018), with an "amber light" threshold at M_L 0.0 and a "red light" threshold at M_L 0.5. An amber event during injection requires well pressures to be reduced, though the stage can continue; a red-light event requires injection to stop, while seismicity is monitored for at least 18 h, after which injection may restart once levels of seismicity have subsided below M_L 0.5 (Cuadrilla Resources Ltd., 2019). These thresholds are the most conservative to be used in the regulation of HF or any comparable operations such as geothermal, anywhere in the world (Baisch *et al.*, 2019; Kendall *et al.*, 2019), reflecting the overall objective of the Oil and Gas Authority to minimize the occurrence of felt events, and to prevent the possibility of damaging events (Clarke, Verdon, *et al.*, 2019).

In 2018 CRL drilled two horizontal wells into the Bowland Shale at the Preston New Road well site, approximately 4 km to the south of Preese Hall. The first of these wells, Preston New Road (PNR)-1z, was stimulated in late 2018. Six events with magnitudes larger than M_L 0.5 occurred, entailing pauses in operations under the TLS. The largest event to occur had a magnitude of M_L 1.5 (Clarke, Verdon, *et al.*, 2019; Kettlety *et al.*, 2020).

In August 2019, CRL commenced the stimulation of the PNR-2 well, which lies approximately 200 m shallower, and 200 m to the north of the PNR-1z well (Fig. 1). However, operations were halted after the occurrence of an M_L 2.9 event at 08:30 British Summer Time on August 26, three days after the latest stage of injection had been completed. The United Kingdom Government has subsequently imposed a moratorium on HF, pending further scientific analysis (BEIS, Oil and Gas Authority *et al.*, 2019). As the first onshore HF site in the United Kingdom since 2011, the PNR wells were closely monitored, including surface and downhole microseismic arrays, monitoring of surface and groundwater chemistry, air quality control, and local traffic monitoring, operated by both CRL and the British Geological Survey.

The effectiveness of TLSs as a method to mitigate HF-IS is the subject of ongoing debate and research (Bosman *et al.*, 2016; Baisch *et al.*, 2019; Clarke, Verdon, *et al.*, 2019). Statistics-based maximum magnitude forecasting based on microseismic observations provides an alternative method of real-time analysis and operational decision-making. Like tectonic earthquakes, HF-IS is typically observed to follow the empirical Gutenberg–Richter (GR) distribution (van der Elst

et al., 2016) with the number of events as a function of magnitude following a power-law distribution (Gutenberg and Richter, 1944). This can be combined with the observation that the total number of events (Shapiro *et al.*, 2010) or cumulative seismic moment (Hallo *et al.*, 2014) scales with the total injected volume. Therefore, the current rate of induced seismicity as a function of injection volume can be extrapolated to the planned total volume to be injected, from which the maximum expected magnitude of an event in the population can be estimated using the GR distribution. The real-time application of these methods relies on the assumption that the statistical parameters used to characterize the seismicity induced during injection seismicity—the GR *b*-value and the scaling between injection volume and seismic moment release—will not change during injection or will change sufficiently slowly such that changes can be acted upon by adjusting or terminating injection. In effect, for these methods to be functional, they assume that higher magnitude seismicity that is symptomatic of fault activation (as opposed to hydraulic fracture growth) can be detected prior to large events occurring and quickly enough to enable some proactive measure to be taken. Kwiatek *et al.* (2019) demonstrated the use of this approach to guide operational decision-making at a geothermal project in Helsinki, Finland. Clarke, Verdon, *et al.* (2019) adopted this approach to guide decision making during the stimulation of the PNR-1z well in 2018, forecasting the M_L 1.5 trailing event that occurred.

In this study, we describe, in detail, the HF-IS that occurred during stimulation of the Preston New Road PNR-2 well in August 2019. We show how the spatiotemporal evolution of the microseismicity images the activation of the fault on which the largest events occurred, and how this structure relates to the fault zone encountered by the previous operations at the site (Clarke, Verdon, *et al.*, 2019). We then examine the changes in magnitude distributions and seismicity rates between injection stages and show how the maximum magnitude forecasting methods were again tested during real-time operations.

Variability in the behavior of induced seismicity has been linked to the relative orientations of faults and stresses (e.g., Göbel, 2015), with high-magnitude seismicity more likely to occur on faults better oriented for failure in the regional stress field (Keranen *et al.*, 2013; Alt and Zoback, 2017; Schoenball *et al.*, 2018; Skoumal *et al.*, 2019). We conclude this article by comparing the orientations of the two faults that reactivated during stimulation of PNR-1z and PNR-2 operations within the regional tectonic stresses, showing that differences in fault stability are likely to have contributed to the differences in fault activation behavior between the two operations.

HF at Preston New Road

The Preston New Road site consists of two horizontal wells, drilled to 2.1 and 2.3 km depth into the Upper and Lower Bowland Shale, a thick (~1.2 km at the PNR site) natural gas-bearing formation that extends across the north of England (Andrews, 2013; Clarke *et al.*, 2018). The wells are located in the south of the Fylde peninsula, northwest England, near the town of Blackpool, Lancashire. The first and deeper horizontal well was drilled into the lower bowland formation and is denoted PNR-1z (Fig. 1). The second well, drilled in the upper bowland formation, approximately 200 m above and to the north of PNR-1z, is denoted PNR-2. PNR-1z was hydraulically fractured between October and December 2018, and monitored by a surface array of 11 broadband seismometers and short-period instruments, and 24 downhole geophones placed in the PNR-2 well (figs. 1 and 3 of Clarke, Verdon, *et al.*, 2019).

HF of PNR-2 began in August 2019. Monitoring was provided by a broadband surface array similar to that used during PNR-1z operations, supplemented by an additional eight accelerometer sites (array geometry shown in fig. 1 of Clarke, Verdon, *et al.*, 2019). Downhole monitoring was provided by 12 geophones installed in the build section (i.e., where the well deviates from vertical to horizontal) of PNR-1z (Fig. 1), placing them such that the array straddled the depth at which injection took place, thereby minimizing event location uncertainties (e.g., Maxwell, 2011).

Geological and geomechanical conditions at the PNR site

The geology at the PNR site has been well constrained from a combination of 3D reflection seismic data, wireline well logs in the vertical PNR-1 well, and logging while drilling data from the horizontal portions of the PNR-1z and PNR-2 wells. In the Lower Bowland Formation targeted by PNR-1z, glacio-eustatic sea-level changes produced clay-rich high-stand packages interlayered with carbonate-rich turbidite packages (Clarke *et al.*, 2018). The clay-rich high-stand packages have elevated gamma-ray values in well logs, which can be correlated to high-impedance layers in the reflection seismic data, whereas the carbonate-rich packages have reduced gamma-ray values that can be correlated to low-impedance seismic layers. In contrast, the upper bowland formation targeted by the PNR-2 well has a more diffuse seismic character, and only its upper and lower boundaries are well imaged in the reflection seismic data. However, its gamma-ray log character contains similarly contrasting packages that are easily identifiable through the sequence. These lithological variations will create geomechanical boundaries that could act to inhibit the vertical growth of hydraulic fractures (e.g., Teufel and Clark, 1984).

PNR-2 hydraulic fracturing operations

The first six stages were pumped without a felt seismic response from 15 to 21 August 2019. However, approximately 4 hr after the end of stage 6, an event with M_L 1.6 occurred, followed by an M_L 1.0 event the following day, just under 24 hr after injection had ceased. The seventh stage was pumped on the 23 August with a reduced injection volume and increased

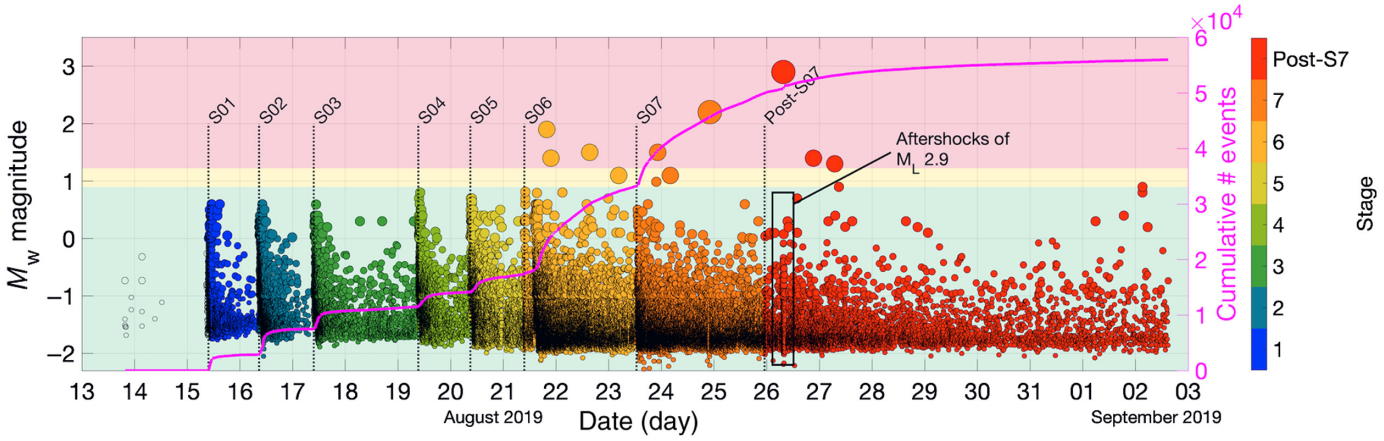

Figure 2. Evolution of seismicity for operations at PNR-2. Background colors show the United Kingdom traffic light system thresholds converted from local magnitude into moment magnitude via the M_w–M_L relationship developed using data from the previous operation at PNR (Cuadrilla Resources Ltd., 2019). The start of pumping each stage is highlighted by dotted lines and is accompanied by an increased rate of measured seismicity. This is visible in the magenta line showing the cumulative number of events. Events prior to stage 1 (S01) are the result of low-volume injection tests through sleeve 1 of PNR-2. After stage 6 (S06) the magnitude of events markedly increases, indicating the interaction between injection and the fault zone. Events are denoted to be "Post-Stage 7" two days after the stage was injected. The M_L 2.9 occurred more than 60 hr after the injection of stage 7. The small number of events that took place before stage 1 was the result of injection tests through sleeve 1. The color version of this figure is available only in the electronic edition.

fluid viscosity, with the intention of limiting the spatial extent of fracture growth and thereby reducing the likelihood of interacting with the area in which all the $M_L > 0.0$ events had occurred. Using a higher viscosity fluid, such as gel, has been shown to reduce the likelihood of induced seismicity during HF in the central United States (Ries *et al.*, 2020).

No $M_L > 0$ events were recorded during the injection of this seventh stage. However, several hours after the stage had been completed, an M_L 1.1 event was recorded, and this was followed by an M_L 2.1 event on the 24 August, and an M_L 2.9 event on 26 August. The full temporal evolution of the seismicity is shown in Figure 2. In total 55,555 microseismic events were detected and located by the downhole array during fracturing operations.

Real-time processing of microseismicity was conducted by a service company, providing event locations, moment magnitudes, source radii, etc. A coalescence microseismic mapping technique was used to locate the events (Drew *et al.*, 2013). The velocity model used for event location was developed using vertical seismic profile and sonic well log data, and the model was calibrated using four downhole "shots" placed at equal distances along the lateral portion of the PNR-2 well. In the following maps of event locations, we only show the 28,000 events for which the signal-to-noise ratio was greater than five.

For these events, error ellipsoids had an average maximum extent of 70 ± 20 m, predominantly oriented in the north–south direction. Errors in the east–west and vertical directions were, on average, around 25 ± 10 m, typical of downhole microseismic monitoring (Jones *et al.*, 2010). During stimulation of both PNR-1z (Clarke, Verdon, *et al.*, 2019; Kettlety *et al.*, 2020) and PNR-2 wells, the locations of the initial events were located around the active injection ports, extending away from these positions as injection progressed. This provides a clear indication that locations are accurate. Similarly, we do not observe any smearing of locations around the axis of the monitoring array, as might be expected if the azimuthal component of the location were poorly constrained (e.g., Eisner *et al.*, 2010). As such, we conclude that the event locations are robust. The downhole locations are consistent with those produced from the surface monitoring array, albeit the surface locations have significantly higher uncertainties (Kettlety *et al.*, 2020).

Moment magnitudes, M_w, were measured both on the surface and downhole arrays using the spectral amplitudes of the *P*- and *S*-wave arrivals, following the method described by Stork *et al.* (2014). The TLS is operated using local magnitudes, with M_L values calculated using the maximum amplitude of the *S* wave measured on the surface array using the updated United Kingdom local-magnitude scale (Luckett *et al.*, 2019), which has been adjusted to account for the close proximity of sources and receivers (Butcher *et al.*, 2017). A relation between M_L and M_w recorded on the surface array was developed by the operator using data from PNR-1z (Cuadrilla Resources Ltd., 2019), which is consistent with the PNR-2 observations (see supplemental material to this article, Fig. S1). This corrects for the derivation between local and moment magnitude scales at low magnitudes (Deichmann, 2006, 2017), which results from a preferential decay of high-frequency energy that adversely affects M_L (Butcher *et al.*, 2020).

Consistent characterization of magnitudes between surface and downhole arrays has, however, presented a challenge at this site (Clarke, Verdon, *et al.*, 2019): smaller events are

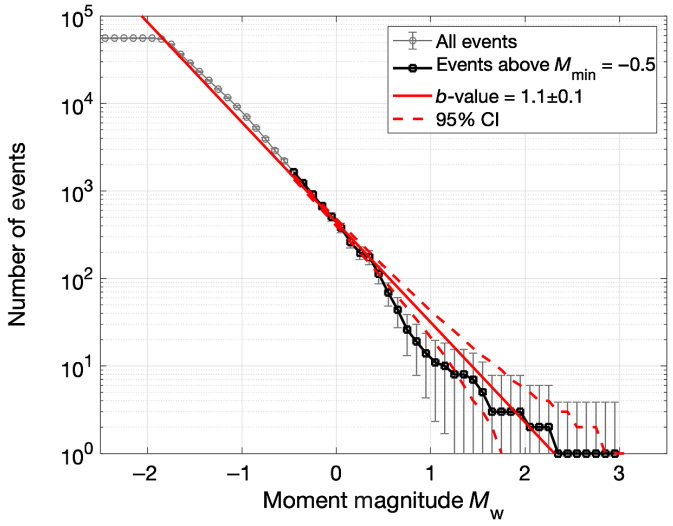

Figure 3. Magnitude frequency distribution for the PNR-2 event population. Overall, events follow the expected GR distribution (Gutenberg and Richter, 1944), but the largest events fall above the frequency expected from the modeled distribution, shown by the red line. The gray error bars for each magnitude bin show the 95% confidence limits for the number of events we would expect drawn from a χ^2 distribution, with the number of degrees of freedom specified as the cumulative number of events, and the red dashed lines show the Poisson 95% confidence limits on the modeled distribution (Naylor *et al.*, 2009). The observations of the largest events do, however, fall within the uncertainties on the modeled distribution. The color version of this figure is available only in the electronic edition.

not visible on the surface array, whereas the amplitudes of larger events tend to be clipped on the downhole array, and furthermore the downhole geophones do not have the low-frequency response to fully characterize larger (and therefore lower corner-frequency) events (e.g., Viegas *et al.*, 2012). Baptie *et al.* (2020) describe how discrepancies in magnitudes between downhole and surface arrays have been addressed—this is discussed at length in the supplemental material (Text S1; Figs. S1 and S2).

The magnitude-frequency distribution for the population is shown in Figure 3, in which we observe a b-value for the overall event population of 1.1 ± 0.1. The b-value and its 2σ (~95%) uncertainty are calculated using the maximum likelihood estimate adapted for binned magnitudes (Aki, 1965; Tinti and Mulargia, 1987; Marzocchi and Sandri, 2003) for events above the minimum magnitude of completeness M_{min}, which we determined by a Kolmogorov–Smirnov goodness-of-fit test (Clauset *et al.*, 2009). It should be noted that the fitted GR distribution slightly overestimates the number of events that occurred in the magnitude range in which the downhole estimates of M_w start to become less robust ($0.5 < M_w < 1.5$). This may be the result of having to combine the downhole and surface catalogs; however, this is clearly necessary to characterize the entire event population. As discussed in the supplemental material, the magnitude corrections of Baptie *et al.* (2020) applied here provide the best combined catalog of moment magnitudes for PNR-2 without full reassessment of the downhole magnitudes, which was not possible at the time of publication. This will be the subject of further study, as this case clearly highlights the difficulties inherent in simultaneously monitoring injection using surface and downhole microseismic arrays.

Evolution of Microseismicity during PNR-2 Operations

Figure 4 shows the key structures that developed or were reactivated during HF of the PNR-2 well, as revealed by microseismic event locations. Figure 5 shows the spatiotemporal evolution of the microseismicity, leading up to the activation of the fault.

Stage 1 was completed with no events exceeding M_L 0, and the majority of events were spatially distributed symmetrically in a 300-m long linear feature centered on the injection point. These were the first events to occur in the center of the "NS Zone" shown in Figure 4. Events extended north-northwest–south-southeast, consistent with the maximum horizontal stress direction, $\theta_H = 173°$ (Clarke, Soroush, and Wood, 2019), and the orientation of HF growth observed during PNR-1z operations. We interpret these events as being indicative of the growth of hydraulic fractures from the well.

Microseismicity during stages 2 and 3 mostly occurred in the same northsouth zone, extending the hydraulic fractures by around 100 m to the north. The magnitude of the largest events increased slightly from stage 1, though all were below M_L 0 and did not exceed the TLS thresholds. These events all took place during or immediately after injection, within the central north–south zone.

Further microseismicity was also observed in two clusters to the west of the main HF zone. The "Western Zone" (Fig. 4) is offset laterally from the toe of the well by approximately 100 m and is at a similar depth to the well. It extended both northward and southward from the well, although it has a somewhat diffuse character. In addition, a number of small events ($M_w < -0.4$) were located to the west of the north–south zone along a north-south striking plane, dipping to the east and extending over 100 m below the injection interval. This structure was located near a feature termed "PNR-1z_i" that was identified during stimulation of the PNR-1z (Cuadrilla Resources Ltd., 2019), although it is above the PNR-1z_i feature, and there is no overlap among event locations. Nevertheless, these events could correspond to reactivation of the same feature, if it extends to a shallower depth. The "Western Zone" may represent further hydraulic fracture development; however, it is not clear why there is a gap in hydraulic fracture growth between the point of injection and this westward zone. This could be the result of a stress shadow forming from the opening of fractures in

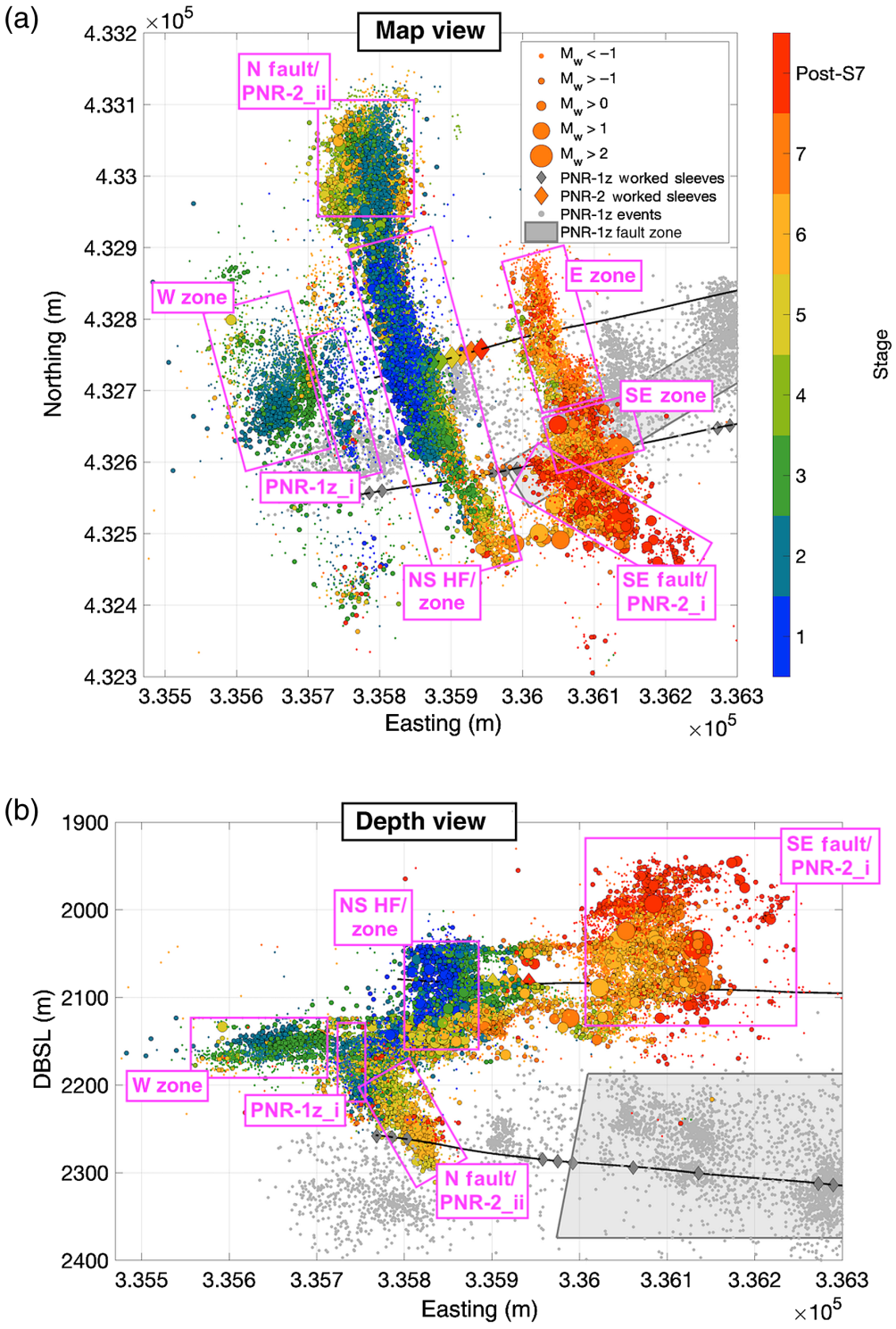

Figure 4. (a) Map view of events recorded up to 13/09/19 with M_w greater than −1.5. Event hypocenters are shown as circles, colored by the stage with which they were associated, and sized by magnitude. The well paths of PNR-1z and PNR-2 are shown as black lines, with PNR-1z to the south of and below PNR-2. (b) East–west depth cross section of the same events. Diamonds show the locations of the sliding sleeves, with sleeves worked during 2018 (PNR-1z) shown in gray, and those worked during 2019 (PNR-2) colored by stage. Gray dots show the hypocenters of the events that occurred during PNR-1z operations, and the gray plane shows the plane of the fault that was activated during those operations (see Clarke, Verdon, *et al.*, 2019). Pink boxes and text annotations indicate the main structures and faults identified in the microseismic data, with the names that are referred to throughout the text. The color version of this figure is available only in the electronic edition.

the central north–south zone (Nagel *et al.*, 2013; Kettlety *et al.*, 2020).

The microseismicity during stage 4 again took place along the north–south zone, indicating further injection into the same hydraulic fracture network. At the northern tip of the north–south zone, around 250 m from the injection point, events began to delineate a feature that extends roughly 130 m below the north–south zone that maps the hydraulic fracture propagation. This structure has a strike that is approximately northward (∼0°) and dips approximately 50° to the east. We interpret these events as resulting from fluid pressure reactivating a small fault. This "N fault" has a similar orientation to some of the seismic discontinuities identified in 3D reflection seismic data (Cuadrilla Resources Ltd., 2019), although it is not co-located with any of these. Although these events appeared to occur on a reactivated structure, none of the events exceeded $M_L > 0$.

In addition, after injection of stage 4, events began to appear further to the east of the injection point, just south of Sleeve 13 of the PNR-2 well. This secondary cluster is detached from the main north–south zone, where the majority of events had occurred thus far. The "Eastern Zone" initiated around 100 m further east along the track of the injection well, 50 m deeper than the well, and propagated southward from it. Prior to stage 5, the feature extended in a small lineament roughly 50 m to the south, with a similar orientation to the main north-south zone, parallel to

θ_H. The orientation and growth of this feature from the well suggest that it was a new zone of hydraulic fracture growth. It is yet unclear why new HF nucleation would take place at a section of the well through which no injection was occurring, rather than at the position of the stage 4 sleeve. It could be a similar stress-shadow effect as suggested earlier, with increased fluid pressure near the well stimulating growth of fractures outside of a zone of quiescence, immediately adjacent to the large hydraulic fractures already created in the north–south zone. This explanation of the eastern zone is by no means a definitive conclusion, and its origin requires further study.

During stage 5, microseismicity continued to occur predominantly along the main north–south zone and the eastward-dipping fault structure at its northern end. More events were also observed along the eastern zone at S13, with events increasing its length both north and south of PNR-2, occurring around 2 hr after injection began. The magnitude of events within this eastern zone remained low, most with $M_w < -1$. Approximately 12 hr after injection of stage 5 had stopped, the eastern zone again grew further to the south, with a population of around 100 low-magnitude ($M_w < -1$) events. We interpret this delayed onset of events as being caused by continued fluid pressure diffusion from the hydraulically stimulated areas reaching a more seismogenic volume of rock to the south of the eastern zone, the "SE Zone," after injection had ceased.

STAGE 6 was pumped in two separate phases on August 21, with the majority of the microseismicity taking place during and after the second, approximately 90-minute phase of injection. During pumping, events again predominantly took place in the central north–south zone, indicating much of the injected fluid was continuing to enter the previously stimulated zone, even though the stage 6 sleeve is over 50 m to the east of this zone (Fig. 5). After injection stopped, significant amounts of microseismicity continued to occur along the length of the eastern zone. Approximately 5 hr after injection, an M_L 1.6 event occurred within the southeast zone. This triggered the TLS red light, suspending any future injection for at least 18 hr. In the two days of observation that followed, 2 more $M_L > 0.5$ events occurred, measuring 0.9 and 1.0, located in the same region within the southeast zone (Fig. 5).

On 23 August CRL injected stage 7, using a reduced fluid volume and an increased fluid viscosity in an attempt to reduce the likelihood of further interaction with any seismogenic regions to the south of the PNR-2 well. During injection, microseismicity was observed mostly along the eastern zone, with a smaller number of events still occurring on the main north–south zone to the west. During injection, no $M_L > 0$ events occurred. Five hours after injection stopped, larger events began to take place within the south–east zone, including an M_L 1.1 event located between the southern tip of the north–south zone and the south–east zone. Over the following two days these southeast zone events continued, including an M_L 0.5 event 14 hr after the end of stage 7, followed by an M_L 2.1 earthquake 33 hr after the end of stage 7.

The M_L 2.9 earthquake

On the morning of 26 August, over 60 hr after the end of stage 7, the M_L 2.9 earthquake occurred. Because of the timing of the event, some three days after pumping operations had ceased, the operator was not required to continuously monitor downhole microseismic on a 24 hr basis, and intermittent data acquisition on the downhole array during the morning of the 26 meant that no downhole data were recorded for a 15 s period prior to and during the M_L 2.9 event. However, this event was well recorded by the surface array. The downhole array was able to capture a burst of microseismicity, immediately after the mainshock, with rates of microseismicity remaining elevated for approximately 1 hr after the M_L 2.9 event.

The locations provided by the surface array are less precise than those from the downhole system (see Kettlety *et al.*, 2020 for a comparison). Therefore, we use the locations of these aftershock events to identify the position of the M_L 2.9 rupture. These are shown in Figure 6: they occurred along a near-vertical plane that extends away from the southeast zone, where the highest levels of seismicity had previously occurred, to the southeast. A least-squares fit to these aftershock events gives a plane with strike of 130° and a dip of 80°. Interestingly, the aftershocks appear to occur around an elliptical zone, the center of which is quiescent (Fig. 6). Our interpretation is that the aftershocks occurred in a "halo" around the softened rupture surface of the M_L 2.9 event, with the aftershocks occurring at the edges of the fault, where stresses will have accumulated during rupture. The plane fitted to the M_L 2.9 aftershock cluster has dimensions of approximately 350 × 250 m, giving a rough fault slip area for the ellipse of approximately 7×10^4 m^2. Assuming that the observed aftershocks represent stress relaxation around the edges of the M_L 2.9 rupture surface, this is considered to be a reasonable estimate for the dimension of the rupture.

For a circular fault, with radius R and area A, seismic moment is related to stress drop $\Delta\sigma$, by:

$$M_o = \frac{16}{7\pi}\Delta\sigma RA. \quad (1)$$

Given a stress drop between 1 and 10 MPa, the approximate rupture area for the M_L 2.9 event, which had measured moment magnitude of M_w 2.9 (see supplemental material), is between 4×10^4 and 2×10^5 m^2 (Madariaga, 1979; Kanamori and Brodsky, 2004), consistent with the area delineated by the aftershocks, as described earlier. This supports our interpretation that the aftershocks occurred in an elliptical "halo" around the softened rupture zone. We term this near-vertical, southeast-striking fault PNR-2_i, hereafter.

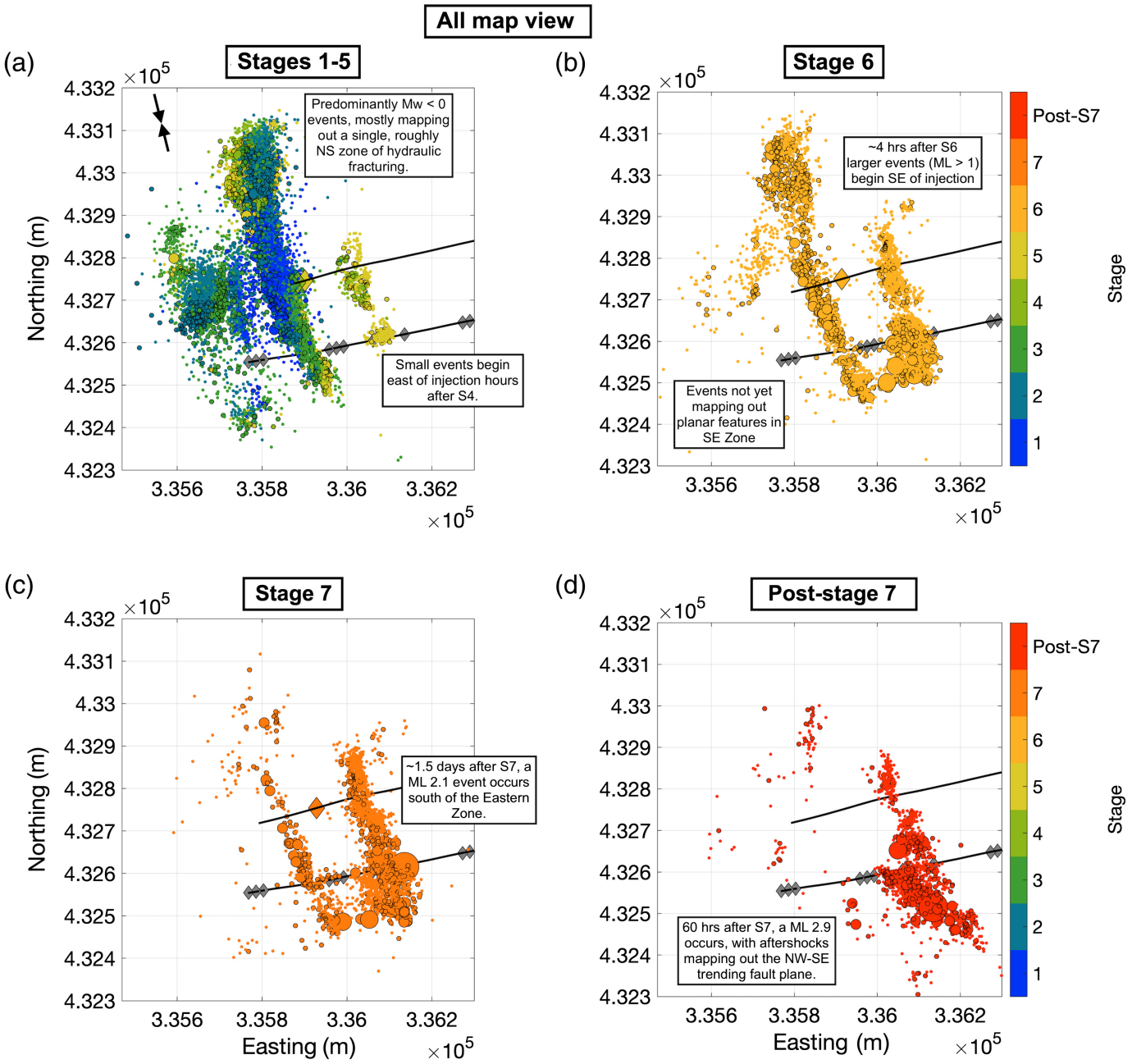

Figure 5. Temporal evolution of microseismicity at PNR-2, using the same symbols, color scheme, and legend as in Figure 4. (a) Map of stages 1–5, (b) Map of stage 6, (c) Map of stage 7 (up to 00:00 on August 26), and (d) seismicity that occurred from 00:00 on the August 26 until the end of the monitoring period. Annotations in black text describe the seismicity that occurred during each of these time periods. The $S_{H\max}$ direction of 170° is shown in panel (a) by the black arrows. The color version of this figure is available only in the electronic edition.

No further injection operations took place after stage 7, and the magnitudes of seismicity subsided. The downhole microseismic array was removed at the end of September 2019, and the measured microseismicity rate was at that time down to around 12 events per day, all measuring below M_w 0.5. More events were detected by the surface array after the M_L 2.9, the last occurring on 6 October 2019, three of which had $M_L \geq 0$, the largest being M_L 0.2.

The focal mechanism for the M_L 2.9 event was determined from surface array data using both the first motion polarities of both the *P* and *S* waves (Hardebeck and Shearer, 2002), as well as the *P*-to-*S*-wave amplitude ratios (Hardebeck and Shearer, 2003; Vavryčuk, 2015). This is shown in Figure 6a. It has a strike of 127°, dip of 84°, and rake of −160°, and thus the orientation of the northwest–southeast nodal plane is consistent with the plane fitted to the aftershocks.

Overall, our interpretation of the observed microseismicity is as follows. During stages 1–5, a hydraulic fracture zone

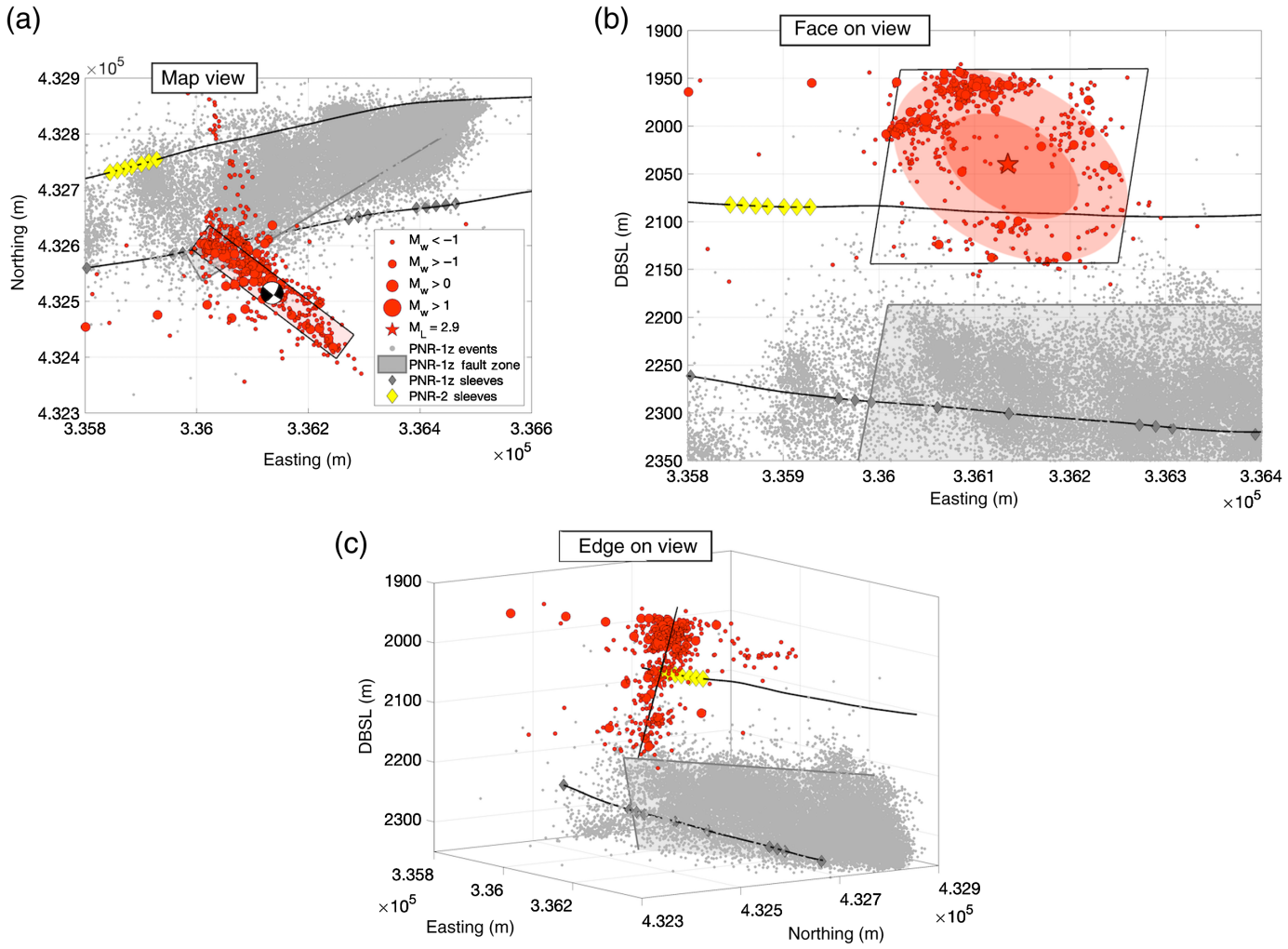

Figure 6. The hypocenters of aftershocks occurring within 1 hour of the M_L 2.9 event, used to delineate the activated PNR-2_i fault. (a) A map view; (b) and (c) Two oblique perspectives of the fault in three dimensions. The lower hemisphere focal mechanism shown in panel (a) is that of the M_L 2.9 earthquake. The plane shown is found by a least square fit to the events in the aftershock cluster. The "halo" annotated in panel (b) highlights the ring of the events around a region of quiescence, with the inferred location of the M_L 2.9 event at its center. This approximately 350 × 250 m ellipse has an area of ~7×10^4 m^2, consistent with the fault area inferred from the moment magnitude of the M_L 2.9 event (~1×10^5 m^2). The color version of this figure is available only in the electronic edition.

extended both to the north and south of the well, along the maximum horizontal stress orientation. At the northern end of this feature, a preexisting structure was intersected, dipping to the east below the zone of operations, but it did not produce significant levels of seismicity. From stage 5, a second zone of HF initiated further to the east, roughly at the position of sleeve 13. The mechanism by which fluid was transferred to initiate fractures at this point remains unclear. This fracture zone propagated to the south, where it eventually intersected a preexisting fault striking to the southeast. As stimulation proceeded, more of the injected fluid entered the eastern fracture zone, with the transfer of pressure to the southeast fault and onset of fault reactivation taking place over a timescale of several hours, such that much of the seismicity occurred after injection of these stages had ceased. After stage 7, prolonged seismicity occurred over several days without further injection, ultimately leading to the M_L 2.9 event, after which seismicity subsided.

Relationship between PNR-1z and PNR-2 seismicity

Figure 6 also shows the microseismicity that occurred during stimulation of the PNR-1z well in 2018 (Clarke, Verdon, *et al.*, 2019), including the northeast striking plane on which most of the larger events occurred, identified as NEF-1 by Clarke, Verdon, *et al.* (2019) (and as PNR-1z_ii by Cuadrilla Resources Ltd, 2019). We find that there is little or no spatial overlap between the two event populations, with the PNR-2 events occurring generally 100 m above the interval stimulated by PNR-1z. The PNR-2_ii fault at the northern end of the main HF zone does extend downward to the depth of PNR-1z events, but this fault is over 400 m to the north of the zone stimulated by PNR-1z.

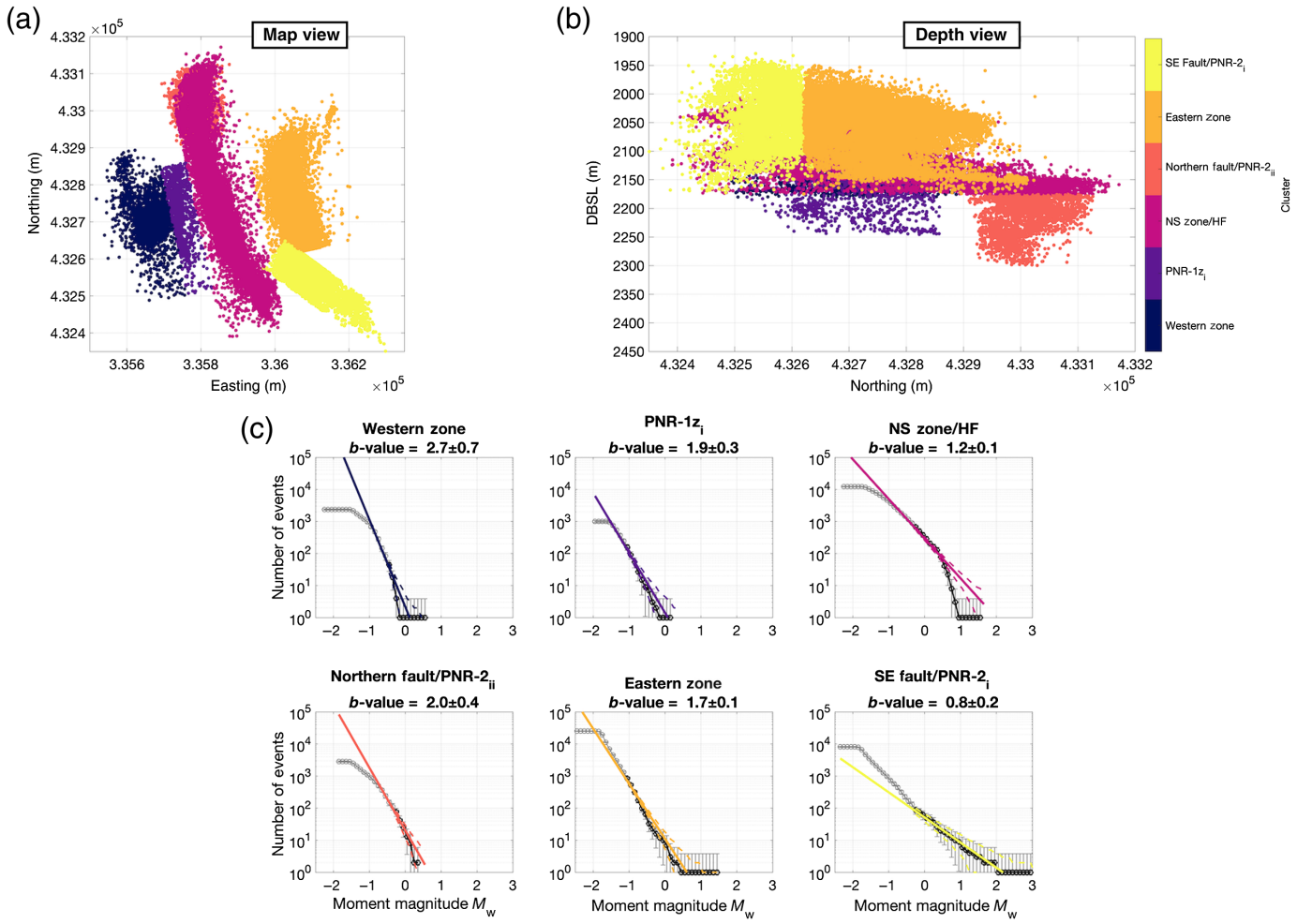

Figure 7. Spatial variation of *b*-values. (a) A map and (b) cross section of all events in the PNR-2 microseismicity catalog, assigned into clusters according to the spatiotemporal evolution of events described above and in Figure 4. (c) Observed magnitude-frequency distributions for each of these zones (light-colored dots for events below the magnitude of completeness, dark for those above) and the GR distribution fit to these observations (colored lines). The southeast (SE) Fault/PNR-2_i fault events have a *b*-value of less than 1, indicating the release of tectonic stresses, whereas all the other zones have *b*-values larger than 1, indicating that events are directly driven by fluid flow and pore pressure effects. The color version of this figure is available only in the electronic edition.

The largest events to occur during PNR-2 operations are found above the southwestern end of the NEF-1 fault plane identified for PNR-1z. This led to an initial supposition that events could have been occurring on a shallower extension of the same feature. However, once the northwest–southeast strike of the reactivated fault was unambiguously delineated by the aftershocks of the M_L 2.9 event, it became clear that seismicity from the two wells occurred on two different faults, because the fault reactivated at PNR-1z had a northeast strike, whereas the fault reactivated at PNR-2 had a southeast strike. We did not observe any microseismicity along the NEF-1 during stimulation of PNR-1z. Evidently, the 200 m vertical and lateral separation between the wells, combined with the geomechanical barriers to hydraulic fracture propagation created by the lithological variabilities described earlier, was sufficient to prevent a linkage from forming between the two stimulated zones.

Microseismic Event Magnitude Distributions

The GR *b*-values of microseismic event populations can provide important information about the nature and style of deformation. Typically, high *b*-values are associated with events driven directly by HF, pore pressure, and fluid flow effects, whereas low *b*-values occur in which tectonic stresses are released on preexisting fault planes (e.g., Verdon *et al.*, 2013). For example, Kettlety *et al.* (2019) used spatial variations in *b*-values to differentiate between events that were directly associated with HF and fluid flow, and events occurring on reactivated faults.

Figure 7 shows the spatial distribution of *b*-values for the PNR-2 microseismicity, calculated using moment magnitude values. We divide the events into spatial clusters based on

the zones described earlier (Fig. 4). For each cluster, we compute the GR b-value using the same method, as previously described, computing the minimum magnitude of completeness, M_C, using Kolmogorov–Smirnov test (Clauset *et al.*, 2009) with a 10% acceptance level.

We find that for the main north–south zone, the western zone, the eastern zone, the PNR-1z_i feature, and the PNR-2_ii fault at the northern end of the north–south zone, the b-values are higher than 1, implying that deformation and microseismicity on these features are driven directly by hydraulic fracture propagation or by associated pressure perturbation and fluid movements (Verdon *et al.*, 2013; Eaton and Maghsoudi, 2015). This is the case even for the PNR-1z_i and PNR-2_ii features, which we interpret as being preexisting structures (Cuadrilla Resources Ltd., 2019). The growth of low-magnitude events along these features may be driven by pore pressure diffusion along a zone of higher permeability relative to the surrounding rock mass or by fracturing along a zone of preexisting weakness. However, it is clear from the b-values, and from the absence of $M_L > 0$ events on these features, that these events do not represent the release of tectonic stresses across larger rupture planes.

In contrast, the southeast zone, which contains the PNR-2_i fault on which the largest event occurred, has a significantly lower b-value. The difference in b-value denotes a fundamental change in physical behavior, indicating that events in this zone are driven more by the release of tectonic stress on a preexisting fault, resulting in the occurrence of larger-magnitude events. During real-time analysis, the evaluation of seismogenic zones presented here was naturally ongoing, and mostly developed post-injection, and thus the shifts in regime presented here were less clear.

The overall magnitude-frequency distribution represents the superposition of the two distinct processes, leading to a flat-tailed, slightly bi-modal distribution. This observation has been made for other HF-IS datasets (Igonin *et al.*, 2018) in which faults have been reactivated. Figure 3 shows the magnitude–frequency distribution for the entire PNR-2 event population, and we observe that the high-magnitude events are larger than expected given the GR distribution observed for the whole population. It is of interest to assess whether this effect is of statistical significance, given the uncertainties inherent in dealing with small numbers of events at the tail of a power-law distribution (e.g., Naylor *et al.*, 2009). With 1634 events larger than a minimum magnitude M_{Min} of −0.5, the expected largest event magnitude, M^M_{MAX}, from the GR distribution is M_w 2.4 (van der Elst *et al.*, 2016), whereas the observed largest event was M_w 2.9. The occurrence of an event with magnitude M_q within a confidence level of q is given by (van der Elst *et al.*, 2016):

$$M_q = M^M_{MAX} - \frac{1}{b}(\log(-\ln q)), \tag{2}$$

giving an M^M_{MAX} plus 1-sigma of M_w 3.1. Thus, although the M_w 2.9 event is larger than the expected M^M_{MAX}, given the distribution of smaller events, it is within the variability we might expect from the GR distribution. In Figure 3, the error bars for each magnitude bin show the 95% confidence limits for the number of events we would expect drawn from a χ^2 distribution, with the number of degrees of freedom specified as the cumulative number of events, and the dashed lines show the Poisson 95% confidence limits on the modeled distribution (Naylor *et al.*, 2009). These show that, although a modeled GR distribution with these a- and b-values gives the largest observed events falling above the model maximum magnitude, these observations fall within the uncertainties of the model distribution. Hence, there is no evidence to suggest that this case represents a runaway rupture event, in which the largest magnitudes fall far above the GR distribution (e.g., Igonin *et al.*, 2018). It must be noted that this is an a posteriori estimate based on the final observed event count and was not made as a forecast during operations, nor does it represent the likelihood of seismicity occurring elsewhere in the Bowland Shale.

Maximum Magnitude Forecasting

As in Clarke, Verdon, *et al.* (2019), we applied statistics-based maximum magnitude forecasting on real-time data acquired during operations at PNR-2, using both the seismic efficiency (S_{EFF}; Hallo *et al.*, 2014) and seismogenic index (SI; Shapiro *et al.*, 2010) methods. The seismic efficiency term S_{EFF} (Hallo *et al.*, 2014) modifies the (McGarr, 1976, 2014) relationship between injected volume ΔV and cumulative seismic moment release ΣM_0, to account for aseismic moment release:

$$\Sigma M_0 = S_{EFF}\mu\Delta V. \tag{3}$$

By measuring the S_{EFF} and b-value during operations, the expected magnitude of the largest event M^M_{MAX} can be estimated (Hallo *et al.*, 2014):

$$M^M_{MAX} = \frac{2}{3}\left(\log\left(\frac{S_{EFF}\mu\Delta V[\frac{3}{2}-b]}{b10^{9.1}}\right)\right) + \frac{2}{3}\log(10^{b\delta} - 10^{-b\delta}), \tag{4}$$

in which δ is the probabilistic bin-size around M^M_{MAX}, which is included to ensure that mathematically, for a range of cumulative seismic moments and magnitudes of completeness M_{Min}, there is only a single event with the largest magnitude (Hallo *et al.*, 2014). Verdon and Budge (2018) found that an extra factor of 0.5 should be added to the M^M_{MAX} found from equation (4) to account for the uncertainty inherent in sampling events from the GR distribution, and ensure a 95% confidence on the forecasted M^M_{MAX}.

The SI of Shapiro *et al.* (2010) proposes a linear scaling between the number N of induced events, larger than a magnitude M, and the injection volume:

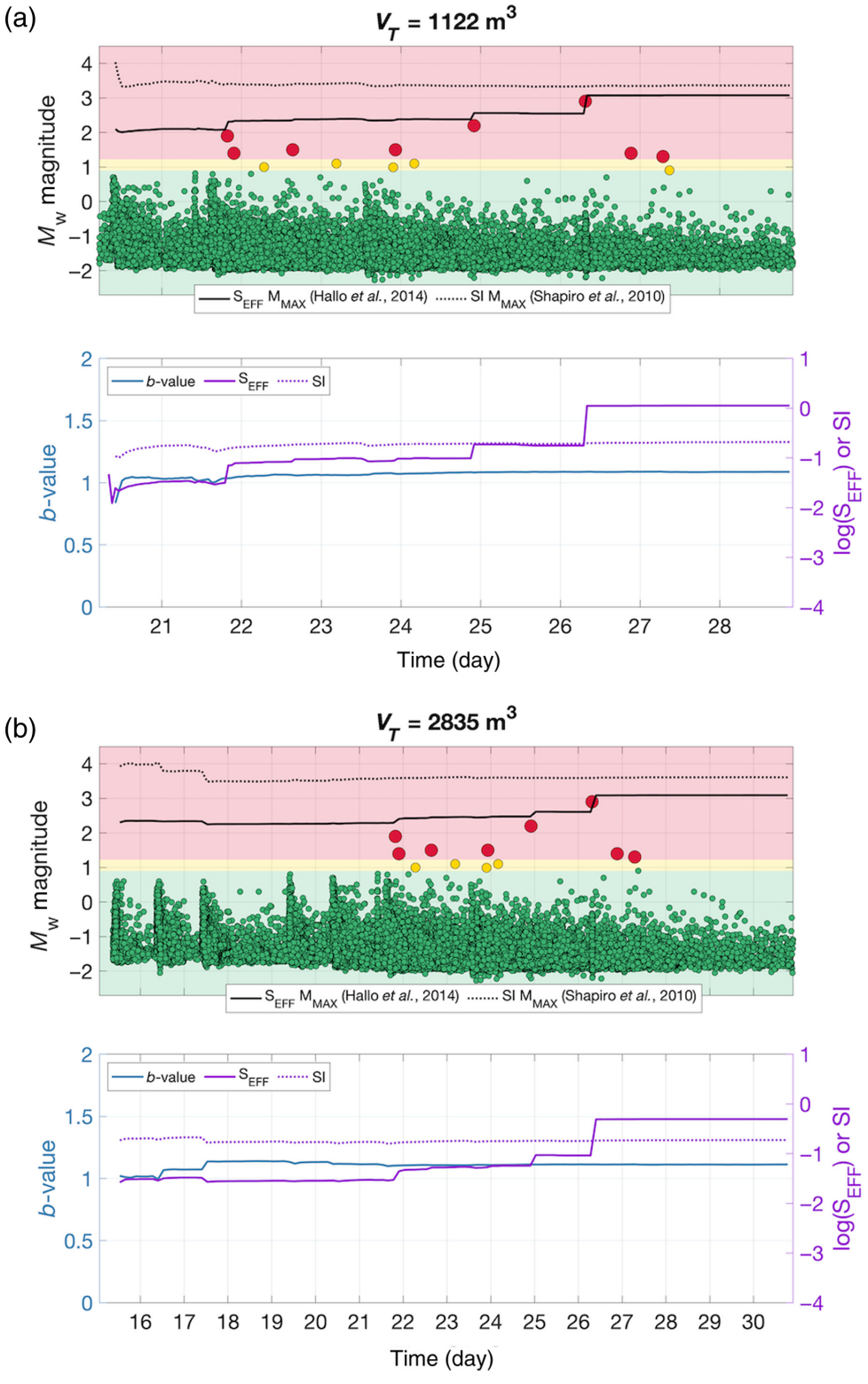

Figure 8. Maximum magnitude forecast when (a) data from stages 5 to 7 are combined, and (b) all PNR-2 event and injection data are combined. Circles show the events, colored by their magnitude with respect to the traffic light scheme thresholds in M_w. The solid black line shows the M^M_{MAX} produced by the S_{EFF} method (Hallo *et al.*, 2014), whilst the dotted line shows the M^M_{MAX} from the SI method (Shapiro *et al.*, 2010). The lower figure for each shows the evolution of the *b*-value (solid blue line), S_{EFF} (solid purple), and *SI* (dotted purple) during operations. In both cases, preceding seismicity did not sufficiently characterize the largest event that went on to take place on the PNR-2_i fault. The color version of this figure is available only in the electronic edition.

$$SI = \log\left(\frac{N(M)}{\Delta V}\right) + bM. \quad (5)$$

For both methods, once the S_{EFF} or *SI* has been calculated from observed data, the expected population of events can be extrapolated for some prospective total volume V_T to be injected. From this, the GR *b*-value is used to then find the largest expected event.

We compute *b*-values using a magnitude of completeness of −1.0, which from both the total and clustered magnitude-frequency distributions is reasonable. We require a minimum of 50 events to compute a *b*-value above this minimum, though this is quickly exceeded during each stage. The *b*-values will be controlled by the distribution at lower magnitudes, as these events are much more numerous. Therefore, they may not incorporate the effects of a bimodal or flat-tailed distribution, as described earlier. The variety of behaviors observed in the PNR-2 microseismicity and their effect on the magnitude frequency distribution therefore poses a challenge for these forecasting methods.

Clarke, Verdon, *et al.* (2019) showed the importance of appropriately apportioning injection volumes when performing correlations between injection volumes and observed seismic rates. For PNR-2, stages 6 and 7 injected fluid into the eastern zone, which presumably transferred pressure to the southeast zone where the largest events occurred. During stage 5, we observed microseismic activity in the eastern zone, but it is not clear whether fluid pressures associated with stage 5 ever reached the southeast zone. Stages 1–4 did not appear

to directly intersect or interact with the eastern features of the PNR-2_i fault. However, we cannot rule out the possibility that the fluid pressure could diffuse from the southern end of the North–south zone and potentially produce a hydraulic connection from the main north–south HF zone to the southeast zone AND PNR-2_i fault.

Therefore, in our forecasting approach we consider a selection of scenarios, including treating each stage as an isolated injection event, combining injection volumes from stages 5 to 7, which generated the eastern zone seismicity that linked to the PNR-2_i fault, and considering all stages cumulatively.

Figures S3–S5 in the supplemental material show the results of the stage-by-stage forecasting, whereby forecasts are produced using injection volumes and events from each stage separately. In this case, the prospective total volume V_T of each forecast is the volume injected during the stage. These forecasts were successful for the first five stages, forecasting M^M_{MAX} in the range of $1.5 < M_{\mathrm{w}} < 2.0$, when using the Hallo *et al.* (2014) S_{EFF} method, and $2 < M_{\mathrm{w}} < 3$, when using the Shapiro *et al.* (2010) *SI* method. As in Verdon and Budge (2018) and Clarke, Verdon, *et al.* (2019), the SI method tends to produce more conservative (i.e., larger) forecasts than S_{EFF}, which are driven by the different scaling exponent assumed between ΔV and ΣM_0: 1.0 for S_{EFF}; and 1.5 for *SI* (Clarke, Verdon, *et al.*, 2019). However, for stage 7, the forecast M^M_{MAX} values during injection were approximately M_{w} 1.3 using S_{EFF} and 2.0 using *SI*, whereas this stage produced events with magnitudes up to M_{w} 2.9 (i.e., the M_{L} 2.9). This reinforces the findings made by Clarke, Verdon, *et al.* (2019), in which multiple injection stages reactivate the same feature, the injected volumes, and the seismicity produced, must be treated cumulatively.

Figure 8a,b, respectively, shows the forecasts when stages 5–7 are combined and when all PNR-2 stages are combined. In both cases the resulting forecasts for stage 6 onward, when the larger events occurred, are similar. The S_{EFF} approach forecasts M^M_{MAX} of approximately 2.1 during stage 6, matching the seismicity that occurred after this stage. The occurrence of trailing events after stage 6 increased the forecast slightly to approximately $M^M_{\mathrm{MAX}} = 2.5$, just after stage 7. However, this represents an under-prediction with respect to the M_{w} 2.9 event that occurred after this stage, though does forecast the other large events (e.g., the M_{L} 2.1). As S_{EFF} rises with the occurrence of larger trailing events, the M^M_{MAX} forecast increases slightly after injection ceased, up to M_{w} 2.6 just prior to the occurrence of the M_{w} 2.9. During real-time analysis, the correction to the downhole M_{w} values discussed in the supplemental material had yet to be applied, further reducing the modeled M^M_{MAX} values that were available for decision making during the operation.

The *SI*-method values were consistently higher, with a forecast of M^M_{MAX} around M_{w} 3.5 during the earlier stages (before any evidence of fault reactivation had occurred), and continuing with $M^M_{\mathrm{MAX}} \sim 3.5$ during and after stage 5. Therefore, this method did predict the largest magnitude event that occurred; however, the evolution of *SI* did not capture the evolution of the system from normal HF to fault reactivation during the latter stages, consistently overestimating the largest magnitude.

However, although the S_{EFF} method did underpredict the observed M^M_{MAX} after stage 6, during real-time monitoring, it was clear from both methods, and from observations of the bimodal, flat-tailed magnitude distribution (Fig. 7), that a change in the seismic response had taken place. The rates of seismicity release were larger than those observed during stimulation of PNR-1z: whereas Clarke, Verdon, *et al.* (2019) report a maximum *SI*value of −1.8, the maximum *SI* value during PNR-2 stages that activated the fault was $SI \sim -0.7$. This implies an order of magnitude more events occurring per unit volume injected. The observed *SI* value of −0.7 is toward the upper end of SI values observed during HF in the WCSB (Verdon and Budge, 2018; Schultz *et al.*, 2018) and in the Sichuan basin, China (Lei *et al.*, 2017).

This change in behavior was not visible during pumping of stage 6, because the interaction with the seismogenic southeast zone took several hours to develop as the pressure propagated outward from the injection point. Until several hours after stage 6, no event had $M_{\mathrm{L}} > 0$, the amber-light threshold of the TLS. This highlights a potential challenge for currently configured real-time control measures for mitigation of induced seismicity. This issue poses as much of an issue to TLSs as it does adaptive measures described earlier, because the seismogenic nature of the zone only became evident after pumping stopped.

Operational steps were taken to mitigate further seismicity during the pumping of stage 7, pumping a stage of only 190 m^3, reduced from approximately 400 m^3 for each of the preceding six stages, and increasing the injected fluid viscosity, such that the pressure pulse would not extend as far from the well, reducing the likelihood of further interaction with the southeast zone. Ries *et al.* (2020) have recently shown a reduced likelihood of induced seismicity when higher-viscosity HF fluids are used.

We, therefore, conclude that the sequence of events at PNR-2 shows that our ability to image and understand seismicity related to hydraulic stimulation is not lacking, but further study is required to better understand how interactions between hydraulic fractures and faults can be modeled and mitigated, and microseismicity understood in real-time during operations.

In Situ Stress Acting on Faults

The NEF-1 fault activated during PNR-1z had dimensions of approximately 500 by 200 m (Clarke, Verdon, *et al.*, 2019; Kettlety *et al.*, 2020), whereas the rupture area of the PNR-2_i fault activated during PNR-2, as delineated by the aftershocks described earlier, had dimensions of 350 by 250 m.

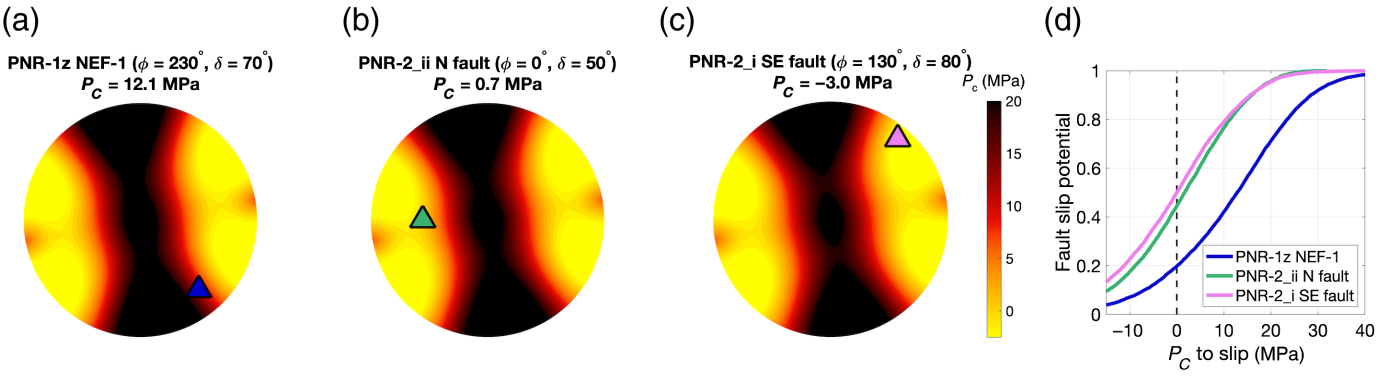

Figure 9. Lower-hemisphere stereographic poles-to-plane projections of critical pore pressure P_C for the two fault depths at PNR. (a) P_C for the northeast (NE)-striking fault of PNR-1z (at a depth of around 2300 m), with the blue triangle showing the orientation of the plane. (b) P_C for the PNR-2_ii (north) fault activated during PNR-2 (at around 2250 m depth), with a green triangle showing its orientation. (c) P_C of the southeast trending PNR-2_i fault as a pink triangle (at ~2300 m depth). The titles in each plot show the P_C value at the orientations of the faults. (d) Cumulative probability curves for failure for a given P_C. The color version of this figure is available only in the electronic edition.

The PNR-1z NEF-1 fault was intersected by around 10 stages of injection, with a combined injection volume of over 1600 m^3 during 2018 operations, whereas the PNR-2 southeast fault was intersected by at the most three stages (stages 5–7), with a combined volume of approximately 1000 m^3. The NEF-1 fault also directly intersected the well and was oriented obliquely with respect to the well path, such that most of its length was within 150 m of active injection stages. The PNR-2_i fault does not intersect the injection well—its closest edge is around 250 m from the nearest injected stage. Hence, the PNR-2_i fault is further from the well, smaller, and received less injected fluid than the PNR-1z NEF-1 fault. However, despite these differences, the largest magnitude event that occurred on the NEF-1 fault (M_L 1.5, Clarke, Verdon, *et al.*, 2019) was significantly smaller than those that occurred on the PNR-2_i fault (M_L 1.6, 2.1, and 2.9, this study).

This disparity in the event magnitudes produced by the two structures can be examined in the context of their orientation with respect to the regional stress field. Clarke, Soroush, and Wood (2019) describe the stress conditions at the Preston New Road site, with gradients of maximum horizontal stress of 0.032 ± 0.006 MPa/m, minimum horizontal stress of 0.016 ± 0.004 MPa/m, vertical stress of 0.025 ± 0.001 MPa/m, pore pressure of 0.013 ± 0.001 MPa/m, and a maximum horizontal stress direction of $\theta_H = 170° \pm 10°$. To assess the stress conditions acting on the identified faults, we compute the in situ stress tensor, and resolve this into normal stress σ_n and shear stress τ on both of the fault orientations, from which we compute the critical pore pressure P_C, required to exceed the Mohr–Coulomb failure envelope (e.g., Chiaramonte *et al.*, 2007; Walsh and Zoback, 2016; Kettlety *et al.*, 2019):

$$P_C = \sigma_n - |\tau|/\varphi, \tag{6}$$

in which φ is the coefficient of friction. We use a generic value of $\varphi = 0.7$ here, which is consistent with previous studies of fault stability and laboratory measurements of shales, including those from the Bowland basin (Harris, 1998; Schoenball *et al.*, 2012; Kohli and Zoback, 2013; Herrmann *et al.*, 2018; Wiseall *et al.*, 2018).

Critical pore pressure can be used as a measure of fault stability (Walsh and Zoback, 2016; Schoenball *et al.*, 2018), in which faults with high P_C require a large amount of pore pressure increase to reach the failure envelope, and faults with low or negative P_C are already close to failure in the given stress field. Faults with low P_C values can be considered critically stressed, with small stress perturbations potentially inducing slip. Figure 9 shows the values of P_C for all orientations at the approximate depths of the three faults clearly activated during PNR operations (2100 m for the PNR-2_i southeast fault, 2250 m for the PNR-2_ii north fault, and 2300 m for the PNR-1z NEF-1 fault), with the triangles showing the lower hemisphere projections of the fault normals.

Figure 9d shows fault slip potential probability curves computed using a Monte Carlo approach (Walsh and Zoback, 2016; Schoenball *et al.*, 2018; Kettlety *et al.*, 2019) assuming uncertainties of ±10° in fault strike and dip, ±50 m in fault depth, and ±0.1 in φ, and the uncertainties in stress gradients described earlier.

The PNR-2_ii feature is relatively well orientated for slip, with P_C of around 1 MPa and would require only a moderate increase in pore pressure to slip. The PNR-1z_i is similarly orientated, and so would have similar P_C values. However, both these features produced a low seismic response, with no events larger than M_L 0.0. The *b*-values for these features are instructive here, with high *b*-values indicating microseismicity driven by pore-pressure effects on a distributed fracture

network, as opposed to the release of tectonic stresses on larger rupture planes. It is, therefore, possible that these features represent zones or corridors of natural fracturing rather than faults, or if they are faults that their frictional properties are such that larger seismogenic ruptures are not able to occur.

The PNR-1z NEF-1 fault has a P_C value of over 10 MPa, meaning it is relatively poorly oriented in the stress field for failure and could only reach the failure envelope given a relatively significant perturbation to the stress state. Events associated with this fault during stimulation of PNR-1z had a low GR *b*-value (Clarke, Verdon, *et al.*, 2019), and did eventually produce an M_L 1.5 event, indicating the release of tectonic stress on a fault plane. However, the M_L 1.5 event only occurred after repeated injection of multiple HF stages directly into the fault. The orientation of this fault plane within the in situ stress field and the resulting high P_C values may explain why.

In contrast, the PNR-2_i southeast fault has a P_C of −3 MPa, with its orientation very near the overall minimum P_C in the stress field. Although a negative P_C value should not be physically possible, because it would imply that slip would be occurring prior to injection, such an observation can be explained as an artifact of stress orientation and gradient uncertainties, or the assumption of zero coherence in performing the calculation, because a positive P_C value can be obtained within acceptable ranges, as shown by the Monte Carlo analysis in Figure 9d, or by assuming a nonzero coherence. Nevertheless, the P_C value for this fault is probably very close to zero, implying that a very small perturbation is sufficient for slip. This would explain why the PNR-2_i fault, when compared with the PNR-1z NEF-1 fault, was able to give a significantly larger seismic response (M_L 2.9 vs. M_L 1.5), despite a smaller injection volume (1000 m^3 vs. 1600 m^3), a smaller seismogenic structure (350 m vs. 500 m length), and being further from the well (c.200 m vs. directly intersecting). Several studies have shown the importance of fault orientation within the stress field (e.g., Keranen *et al.*, 2013; Alt and Zoback, 2017; Schoenball *et al.*, 2018; Skoumal *et al.*, 2019), and the comparison between the PNR-1z NEF-1 feature and the PNR-2_i fault demonstrates this explicitly.

Conclusion

We describe the fault activation that occurred during the HF operation at the Preston New Road site, Lancashire, United Kingdom, in 2019. We use the microseismic event locations to interpret the development of seismicity leading up the felt events. After four relatively typical stages of injection, during which hydraulic fractures appeared to be growing along S_{Hmax}, as expected, events began to occur in a disconnected cluster further east along the unworked section of the well, south of sleeve 13 of the PNR-2 well. Two further stages of injection produced more seismicity in this Eastern Zone, with many events occurring hours after injection ceased, implying that diffusion of pore pressure was playing a significant role in initiating seismicity. The final two stages of injection began to stimulate felt seismicity south of the eastern zone, with magnitudes again increasing in the hours after injection. An M_L 1.6 event occurred after stage 6, and the operator significantly reduced injection volumes and increased fluid viscosity for stage 7. However, within 72 hr of stage 7, events with magnitudes of M_L 2.1 and M_L 2.9 occurred in the same region.

The M_L 2.9 event was not directly imaged by the downhole instruments. However, the aftershock locations and the microseismicity which continued over the following days, mapped a planar feature around 350 m long and striking northwest-southeast. This orientation matches that of the focal mechanisms of the largest events, and the spatial dimensions of the aftershocks are consistent with the rupture area for the M_L 2.9 (M_w 2.9) event.

The delay in seismicity between injection and the activity in the clusters, which connected to the fault zone, suggests that the diffusion of increased fluid pressure, reducing normal stress and declamping the fault (Raleigh *et al.*, 1976; Goebel *et al.*, 2015), was the most likely mechanism for fault activation. Although poroelastic stress transfer (Segall and Lu, 2015), elastic stress transfer from prior events (Schoenball *et al.*, 2012; Kettlety *et al.*, 2019) or fracture opening (Kettlety *et al.*, 2020) and aseismic creep (Bhattacharya and Viesca, 2019; Eyre *et al.*, 2019) may have also contributed, further investigation and modeling of the system is required to confirm the extent to which these mechanisms played a role.

The event frequency-magnitude distributions showed an evolution as the injection proceeded. Initial event populations associated with the HF zones (and subsequent pressure dissipation in between injection) had high *b*-values ($b > 1$). However, as the southeast fault zone began to be activated by injection, the magnitude distribution became bimodal, with more large events ($M_w > 0$) than expected from the GR distribution at lower magnitudes. We interpret this as a shift from a HF-dominated regime, to a tectonic faulting regime of seismicity supporting observations of larger events occurring on the PNR-2_i feature. The shift in regime has previously been observed in HF datasets in which fault activation occurs (e.g., Igonin *et al.*, 2018).

Statistical maximum magnitude forecasting is based on scaling between number and size of events with injection volume, extrapolated to a final planned volume, with the expected largest event size then computed from the GR distribution. For these models to be a useful tool to mitigate felt seismicity, they must be able to forecast accurately and allow an operator to react to a change in the nature of the measured seismicity quickly, whilst fluid injection is still occurring. In this case, activity in the fault zone took place several days after injection had ceased, and the seismicity that occurred during injection had sufficiently high overall *b*-values and sufficiently low S_{EFF} that forecasts underpredicted the size of the largest events. That said, the operator was able to identify the increased rate of seismicity relative to previous stages and adjusted the

injection program in an effort to reduce the likelihood of further fault interaction. This adjustment, however, did not result in the prevention of further seismicity. Further consideration of operational actions that could be implemented to prevent interaction with features leading to seismicity is warranted.

There were clear differences in the behavior of fault activation between the triggering of the NEF-1 fault zone during PNR-1z operations and the southeast-striking fault during PNR-2 operations. The 500 m long PNR-1z fault zone obliquely intersected the injection well around halfway along the well's length and had at least 10 stages injected directly into it. However, the largest event it produced had a magnitude of M_L 1.5. In contrast, the 350 m long PNR-2 fault was triggered at a distance of approximately 200 m by three stages of injection yet produced three events with $M_L > 1.5$, including the M_L 2.9 event. Although other factors such as the frictional properties of the two faults cannot be ruled out, the PNR-2 southeast fault is significantly better aligned for failure when compared to the PNR-1z NEF-1 fault zone. The higher slip potential on the southeast fault likely explains the relative ease with which PNR-2 operations triggered a significantly larger event.

Data and Resources

The microseismic catalog for PNR-1z operations is publicly available from the United Kingdom Oil and Gas Authority website (https://www.ogauthority.co.uk/exploration-production/onshore/onshore-reports-and-data/preston-new-road-pnr-1z-hydraulic-fracturing-operations-data/). Similar data for PNR-2 operations will be publicly available from the United Kingdom Oil and Gas Authority in 2020. Stress gradients data were provided in the hydraulic fracture plan for PNR-2, available at https://consult.environment-agency.gov.uk/onshore-oil-and-gas/information-on-cuadrillas-preston-new-road-site/user_uploads/pnr-2-hfp-v3.0.pdf. All websites were last accessed in October 2020.

Acknowledgments

The authors would like to thank Cuadrilla Resources Ltd., and their joint venture partners Spirit Energy and AJ Lucas, for collaboration on and partial funding of the research presented here. The authors would also like to acknowledge Schlumberger Ltd., who conducted the processing of the microseismic data that are presented in this article, and Nanometrics Ltd., who conducted the processing of the surface derived data acquired by Nanometrics Ltd. and the British Geological Survey. T. Kettlety was also supported by the Natural Environment Research Council (NERC) GW4+ Doctoral Training Partnership (Grant Number NE/L002434/1) and the NERC UKUH Challenge Grants SHAPE-UK project (Grant Number NE/R018006/1). J. P. Verdon is supported by NERC (Grant Number NE/R018162/1). A. Butcher's contribution to this work was supported by the United Kingdom Oil and Gas Authority. This work was a product of the Bristol University Microseismicity Projects—a research consortium whose sponsors include several hydrocarbon operators and service providers. The authors would finally like to thank the anonymous reviewers and the Associate Editor for their constructive feedback on the manuscript.

References

Aki, K. (1965). Maximum likelihood estimate of *b* in the formula log N = A-BM and its confidence, *Bull. Earthq. Res. Inst. Univ. Tokyo* **43,** 237–239.

Alt, R. C., and M. D. Zoback (2017). In situ stress and active faulting in Oklahoma, *Bull. Seismol. Soc. Am.* **107,** no. 1, 216–228, doi: 10.1785/0120160156.

Andrews, I. J. (2013). *The Carboniferous Bowland Shale Gas Study: Geology and Resource Estimation*, British Geological Survey for Department of Energy and Climate Change, London, United Kingdom.

Atkinson, G. M., D. W. Eaton, H. Ghofrani, D. Walker, B. Cheadle, R. Schultz, R. Shcherbakov, K. Tiampo, J. Gu, R. M. Harrington, *et al.* (2016). Hydraulic fracturing and seismicity in the Western Canada sedimentary basin, *Seismol. Res. Lett.* **87,** no. 3, 631–647, doi: 10.1785/0220150263.

Baisch, S., C. Koch, and A. Muntendam-Bos (2019). Traffic light systems: To what extent can induced seismicity be controlled?, *Seismol. Res. Lett.* **90,** no. 3, 1145–1154, doi: 10.1785/0220180337.

Bao, X., and D. W. Eaton (2016). Fault activation by hydraulic fracturing in Western Canada, *Science* **354,** no. 6318, 1406–1409, doi: 10.1126/science.aag2583.

Baptie, B., R. Luckett, A. Butcher, and M. J. Werner (2020). *Robust relationships for magnitude conversion of PNR seismicity catalogues*, *Br. Geol. Surv. Open Rept. OR/20/042*, British Geological Survey for Oil and Gas Authority, London, United Kingdom, 32 pp.

BEIS, Oil and Gas AuthorityKwarteng, K., and A. Leadsom (2019). Government ends support for fracking, available at https://www.gov.uk/government/news/government-ends-support-for-fracking (last accessed October 2020).

Bhattacharya, P., and R. C. Viesca (2019). Fluid-induced aseismic fault slip outpaces pore-fluid migration, *Science* **364,** no. 6439, 464–468, doi: 10.1126/science.aaw7354.

Bosman, K., A. Baig, G. Viegas, and T. Urbancic (2016). Towards an improved understanding of induced seismicity associated with hydraulic fracturing, *First Break* **34,** 61–66.

Butcher, A., R. Luckett, J.-M. Kendall, and B. Baptie (2020). Seismic magnitudes, corner frequencies, and microseismicity : Using ambient noise to correct for high-frequency attenuation, *Bull. Seismol. Soc. Am.* **110,** no. 3, 1260–1275, doi: 10.1785/0120190032.

Butcher, A., R. Luckett, J. P. Verdon, J. M. Kendall, B. Baptie, and J. Wookey (2017). Local magnitude discrepancies for near-event receivers: Implications for the U.K. traffic-light scheme, *Bull. Seismol. Soc. Am.* **107,** no. 2, 532–541, doi: 10.1785/0120160225

Chiaramonte, L., M. D. Zoback, J. Friedmann, and V. Stamp (2007). Seal integrity and feasibility of CO_2 sequestration in the teapot dome EOR pilot: Geomechanical site characterization, *Environ. Geol.* **54,** no. 8, 1667–1675, doi: 10.1007/s00254-007-0948-7.

Clarke, H., L. Eisner, P. Styles, and P. Turner (2014). Felt seismicity associated with Shale gas hydraulic fracturing: The first documented example in Europe, *Geophys. Res. Lett.* **41,** no. 23, 8308–8314, doi: 10.1002/2014GL062047.

Clarke, H., H. Soroush, and T. Wood (2019). Preston New Road: The role of geomechanics in successful drilling of the UK's first horizontal Shale gas well, *Society of Petroleum Engineers EUROPEC at the 81st EAGE Annual Conf.*, SPE-195563. London, United Kingdom, 3–6 June 2019.

Clarke, H., P. Turner, R. M. Bustin, N. Riley, and B. Besly (2018). Shale gas resources of the Bowland basin, NW England: A holistic study, *Petrol. Geosci.* **24,** no. 3, 287–322, doi: 10.1144/petgeo2017-066.

Clarke, H., J. P. Verdon, T. Kettlety, A. F. Baird, and J. M. Kendall (2019). "Real-time imaging, forecasting, and management of human-induced seismicity at Preston New Road, Lancashire, England, *Seismol. Res. Lett.* **90,** no. 5, 1902–1915, doi: 10.1785/0220190110.

Clauset, A., C. R. Shalizi, and M. E. J. Newman (2009). Power-law distributions in empirical data, *Soc. Ind. Appl. Math. Rev.* **51,** no. 4, 661–703.

Cuadrilla Resources Ltd. (2019). *Hydraulic Fracture Plan PNR 2*, available at https://consult.environment-agency.gov.uk/onshore-oil-and-gas/information-on-cuadrillas-preston-new-road-site/user_uploads/pnr-2-hfp-v3.0.pdf

Deichmann, N. (2006). Local magnitude, a moment revisited, *Bull. Seismol. Soc. Am.* **96,** no. 4A, 1267–1277, doi: 10.1785/0120050115.

Deichmann, N. (2017). Theoretical basis for the observed break in ML/Mw scaling between small and large earthquakes, *Bull. Seismol. Soc. Am.* **107,** no. 2, 505–520, doi: 10.1785/0120160318.

Deichmann, N., and D. Giardini (2009). Earthquakes induced by the stimulation of an enhanced geothermal system below Basel (Switzerland), *Seismol. Res. Lett.* **80,** no. 5, 784–798, doi: 10.1785/gssrl.80.5.784.

Drew, J., R. S. White, F. Tilmann, and J. Tarasewicz (2013). Coalescence microseismic mapping, *Geophys. J. Int.* **195,** no. 3, 1773–1785, doi: 10.1093/gji/ggt331.

Eaton, D. W., and S. Maghsoudi (2015). 2b... or not 2b? Interpreting magnitude distributions from microseismic catalogs, *First Break* **33**, no. October, 79–86.

Eisner, L., B. J. Hulsey, P. Duncan, D. Jurick, H. Werner, and W. Keller (2010). Comparison of surface and borehole locations of induced seismicity, *Geophys. Prospect.* **58**, no. 5, 809–820, doi: 10.1111/j.1365-2478.2010.00867.x.

Eyre, T. S., D. W. Eaton, D. I. Garagash, M. Zecevic, M. Venieri, R. Weir, and D. C. Lawton (2019). The role of aseismic slip in hydraulic fracturing–induced seismicity, *Sci. Adv.* **5,** no. 8, eaav7172, doi: 10.1126/sciadv.aav7172.

Fasola, S. L., M. R. Brudzinski, R. J. Skoumal, T. Langenkamp, B. S. Currie, and K. J. Smart (2019). Hydraulic fracture injection strategy influences the probability of earthquakes in the Eagle Ford shale play of South Texas, *Geophys. Res. Lett.* **46,** no. 22, 12958–12967, 10.1029/2019GL085167

Göbel, T. (2015). A comparison of seismicity rates and fluid-injection operations in Oklahoma and California: Implications for crustal stresses, *Lead. Edge* **34,** no. 6, 640–648, doi: 10.1190/tle34060640.1.

Goebel, T. H. W., E. Hauksson, F. Aminzadeh, and J. Ampuero (2015). An objective method for the assessment of fluid injection induced seismicity and application to tectonically active regions in Central California, *J. Geophys. Res.* **120,** 7013–7032, doi: 10.1002/2015JB011895.

Green, C. A., P. Styles, and B. Baptie (2012). *Preese Hall Shale Gas Fracturing: Review and Recommendations for Induced Seismic Mitigation*, Department of Energy and Climate Change, London, United Kingdom.

Grigoli, F., S. Cesca, A. P. Rinaldi, A. Manconi, J. A. López-Comino, J. F. Clinton, R. Westaway, C. Cauzzi, T. Dahm, and S. Wiemer (2018). The November 2017 Mw 5.5 Pohang Earthquake: A possible case of induced seismicity in South Korea, *Science* **360,** no. 6392, 1003–1006, doi: 10.1126/science.aat2010.

Gutenberg, B., and C. F. Richter (1944). Frequency of earthquakes in California, *Bull. Seismol. Soc. Am.* **34,** 185–188.

Hallo, M., I. Oprsal, L. Eisner, and M. Y. Ali (2014). Prediction of Magnitude of the largest potentially induced seismic event, *J. Seismol.* **18,** no. 3, 421–431, doi: 10.1007/s10950-014-9417-4.

Hardebeck, J. L., and P. M. Shearer (2002). A new method for determining first-motion focal mechanisms, *Bull. Seismol. Soc. Am.* **92,** no. 6, 2264–2276, doi: 10.1785/0120010200.

Hardebeck, J. L., and P. M. Shearer (2003). Using S/P amplitude ratios to constrain the focal mechanisms of small earthquakes, *Bull. Seismol. Soc. Am.* **93,** no. 6, 2434–2444, doi: 10.1785/0120020236.

Harris, R. A. (1998). Introduction to special section: Stress triggers, stress shadows, and implications for seismic hazard, *J. Geophys. Res.* **103,** no. B10, 24347–24358, doi: 10.1029/98JB01576.

Herrmann, J., E. Rybacki, H. Sone, and G. Dresen (2018). Deformation experiments on Bowland and Posidonia Shale—Part I: Strength and Young's modulus at ambient and in situ p c–T conditions, *Rock Mech. Rock Eng.* **51,** no. 12, 3645–3666, doi: 10.1007/s00603-018-1572-4.

Holland, A. A. (2013). Earthquakes triggered by hydraulic fracturing in South-Central Oklahoma, *Bull. Seismol. Soc. Am.* **103,** no. 3, 1784–1792, doi: 10.1785/0120120109.

Igonin, N., M. Zecevic, and D. W. Eaton (2018). Bilinear magnitude-frequency distributions and characteristic earthquakes during hydraulic fracturing, *Geophys. Res. Lett.* **45,** no. 23, 12866–12874, doi: 10.1029/2018GL079746.

Jones, G. A., D. Raymer, K. Chambers, and J. M. Kendall (2010). Improved microseismic event location by inclusion of a priori dip particle motion: A case study from Ekofisk, *Geophys. Prospect.* **58,** no. 5, 727–737, doi: 10.1111/j.1365-2478.2010.00873.x.

Kao, H., R. Visser, B. Smith, and S. Venables (2018). Performance assessment of the induced seismicity Traffic light protocol for Northeastern British Columbia and Western Alberta, *Lead. Edge* **37,** no. 2, 117–126, doi: 10.1190/tle37020117.1.

Kanamori, H., and E. E. Brodsky (2004). The physics of earthquakes, *Rep. Prog. Phys.* **67,** 1429–1496, doi: 10.1088/0034-4885/67/8/R03.

Kendall, J. - M., A. Butcher, A. L. Stork, J. P. Verdon, and R. Luckett (2019). How big is a small earthquake ? Challenges in determining microseismic magnitudes, *First Break* **37,** 51–56.

Keranen, K. M., H. M. Savage, G. A. Abers, and E. S. Cochran (2013). Potentially induced earthquakes in Oklahoma, USA: Links between wastewater injection and the 2011 Mw 5.7 earthquake sequence, *Geology* **41,** no. 6, 699–702, doi: 10.1130/G34045.1.

Kettlety, T., J. P. Verdon, M. J. Werner, and J. M. Kendall (2020). Stress transfer from opening hydraulic fractures controls the distribution of induced seismicity, *J. Geophys. Res.* **125**, e2019JB018794, doi: 10.1029/2019JB018794.

Kettlety, T., J. P. Verdon, M. J. Werner, J. M. Kendall, and J. Budge (2019). Investigating the role of elastostatic stress transfer during hydraulic fracturing-induced fault activation, *Geophys. J. Int.* **217,**1200–1216, doi: 10.1093/gji/ggz080.

Kim, K.-H., J.-H. Ree, Y.-H. Kim, S. Kim, S. Y. Kang, and W. Seo (2018). Assessing whether the 2017 Mw 5.4 Pohang Earthquake in South Korea was an induced event, *Science* **360,** no. 6392, 1007–1009, doi: 10.1126/science.aat6081.

Kohli, A. H., and M. D. Zoback (2013). Frictional properties of shale reservoir rocks, *J. Geophys. Res.* **118,** no. 9, 5109–5125, doi: 10.1002/jgrb.50346.

Kwiatek, G., T. Saarno, T. Ader, F. Bluemle, M. Bohnhoff, M. Chendorain, G. Dresen, P. Heikkinen, I. Kukkonen, P. Leary, *et al.* (2019). Controlling fluid-induced seismicity during a 6.1-km-deep geothermal stimulation in Finland, *Sci. Adv.* **5,** no. 5, eaav7224, doi: 10.1126/sciadv.aav7224.

Lei, X., D. Huang, J. Su, G. Jiang, X. Wang, H. Wang, X. Guo, and H. Fu (2017). Fault reactivation and earthquakes with magnitudes of up to Mw4.7 induced by shale-gas hydraulic fracturing in Sichuan Basin, China, *Sci. Rep.* **7,** no. 1, 7971, doi: 10.1038/s41598-017-08557-y.

Luckett, R., L. Ottemöller, A. Butcher, and B. Baptie (2019). Extending local magnitude ML to short distances, *Geophys. J. Int.* **216,** no. 2, 1145–1156, doi: 10.1093/gji/ggy484.

Madariaga, R. (1979). On the relation between seismic moment and stress drop in the presence of stress and strength heterogeneity, *J. Geophys. Res.* **84,** no. B5, 2243–2250, doi: 10.1029/JB084iB05p02243.

Marzocchi, W., and L. Sandri(2003). A review and new insights on the estimation of the b-value and its uncertainty, *Ann. Geophys.* **46,** no. 6, 1271–1282, doi: 10.4401/ag-3472.

Maxwell, S. (2011). Microseismic hydraulic fracture imaging: The path toward optimizing shale gas production, *The Leading Edge* **30,** no. 3, 340–346, doi: 10.1190/1.3567266.

McGarr, A. (1976). Seismic moments and volume changes, *J. Geophys. Res.* **81,** no. 8, 1487–1494, doi: 10.1029/jb081i008p01487.

McGarr, A. (2014). Maximum magnitude earthquakes induced by fluid injection, *J. Geophys. Res.* **119,** 1008–1019, doi: 10.1002/2013JB010597.

Meng, L., A. Mcgarr, L. Zhou, and Y. Zang (2019). An investigation of seismicity induced by hydraulic fracturing in the Sichuan Basin of China based on data from a temporary seismic network, *Bull. Seismol. Soc. Am.* **109,** no. 1, 348–357, doi: 10.1785/0120180310.

Nagel, N., F. Zhang, M. Sanchez-Nagel, B. Lee, and A. Agharazi (2013). Stress shadow evaluations for completion design in unconventional plays, *SPE Unconventional Resources Conf.*, SPE167128, Calgary, Canada, 10–12 April 2013.

National Research Council (2012). *Induced Seismicity Potential in Energy Technologies*, National Research Council, Washington, D.C., doi: 10.17226/13355.

Naylor, M., J. Greenhough, J. McCloskey, A. F. Bell, and I. G. Main (2009). Statistical evaluation of characteristic earthquakes in the frequency-magnitude distributions of Sumatra and other subduction zone regions, *Geophys. Res. Lett.* **36,** no. 20, 1–5, doi: 10.1029/2009GL040460.

Oil and Gas Authority (2018). Consolidated onshore guidance, *Version 2.2*.

Raleigh, C. B., J. H. Healy, and J. D. Bredehoeft (1976). An experiment in earthquake control at Rangely, Colorado, *Science* **191,** 1230–1237.

Ries, R., M. R. Brudzinski, R. J. Skoumal, and B. S. Currie (2020). Factors influencing the probability of hydraulic fracturing-induced seismicity in Oklahoma, *Bull. Seismol. Soc. Am.*, doi: 10.1785/0120200105.

Roth, M. P., A. Verdecchia, R. M. Harrington, and Y. Liu (2020). High-resolution imaging of hydraulic-fracturing-induced earthquake clusters in the Dawson-Septimus area, Northeast British Columbia, Canada, *Seismol. Res. Lett.*, doi: 10.1785/0220200086.

Schoenball, M., C. Baujard, T. Kohl, and L. Dorbath (2012). The role of triggering by static stress transfer during geothermal reservoir stimulation, *J. Geophys. Res.* **117,** no. 9, 2–13, doi: 10.1029/2012JB009304.

Schoenball, M., F. R. Walsh, M. Weingarten, and W. L. Ellsworth (2018). How faults wake up: The Guthrie-Langston, Oklahoma earthquakes, *Lead. Edge* **37,** no. 2, 100–106, doi: 10.1190/tle37020100.1.

Schultz, R., G. Atkinson, D. W. Eaton, Y. J. Gu, and H. Kao (2018). Hydraulic fracturing volume is associated with induced earthquake productivity in the Duvernay play, *Science* **359,** no. 6373, 304–308, doi: 10.1126/science.aao0159.

Schultz, R., V. Stern, M. Novakovic, G. Atkinson, and Y. J. Gu (2015). Hydraulic fracturing and the Crooked Lake sequences: Insights gleaned from regional seismic networks, *Geophys. Res. Lett.* **42,** 2750–2758, doi: 10.1002/2015GL063455.

Segall, P., and S. Lu (2015). Injection-induced seismicity: Poroelastic and earthquake nucleation effects, *J. Geophys. Res.* **120,** 5082–5103, doi: 10.1002/2015JB012060.

Shapiro, S. A., C. Dinske, C. Langenbruch, and F. Wenzel (2010). Seismogenic index and magnitude probability of earthquakes induced during reservoir fluid stimulations, *Lead. Edge* **29,** no. 3, 304–309, doi: 10.1190/1.3353727.

Skoumal, R. J., J. Ole Kaven, and J. I. Walter (2019). Characterizing seismogenic fault structures in Oklahoma using a relocated template-matched catalog *Seismol. Res. Lett.* **90,** no. 4, 1535–1543, doi: 10.1785/0220190045.

Skoumal, R. J., R. Rosamiel, M. R. Brudzinski, A. J. Barbour, and B. S. Currie (2018). Earthquakes induced by hydraulic fracturing are pervasive in Oklahoma, *J. Geophys. Res.* **123,** no. 12, 10918–10935, doi: 10.1029/2018JB016790.

Stork, A. L., J. P. Verdon, and J. M. Kendall (2014). The robustness of seismic moment and magnitudes estimated using spectral analysis, *Geophys. Prospect.* **62,** no. 4, 862–878, doi: 10.1111/1365-2478.12134.

Stork, A. L., J. P. Verdon, and J. M. Kendall (2015). The Microseismic response at the In Salah Carbon Capture and Storage (CCS) site, *Int. J. Greenhouse Gas Control* **32,** 159–171, doi: 10.1016/j.ijggc.2014.11.014.

Teufel, L. W., and J. A. Clark (1984). Hydraulic-fracture propagation in layered rock: Experimental studies of fracture containment, United States Department of Energy, available at https://www.osti.gov/servlets/purl/6567524 (last accessed October 2020).

Tinti, S., and F. Mulargia (1987). Confidence intervals of b values for grouped magnitudes, *Bull. Seismol. Soc. Am.* **77,** no. 6, 2125–2134, available at https://pubs.geoscienceworld.org/bssa/article-lookup/77/6/2125 (last accessed October 2020).

van der Baan, M., and F. J. Calixto (2017). Human-induced seismicity and large-scale hydrocarbon production, *Geochem. Geophys. Geosyst.* **18,** 2467–2485, doi: 10.1002/2017GC006915.

van der Elst, N. J., M. T. Page, D. A. Weiser, T. H. W. Goebel, and S. M. Hosseini (2016). Induced earthquake magnitudes are as large as (statistically) expected, *J. Geophys. Res.* **121,** 4575–4590, doi: 10.1002/2016JB012818.

Vavryčuk, V. (2015). Inversion for the composite moment tensor, *Bull. Seismol. Soc. Am.* **105,** no. 6, 3024–3035, doi: 10.1785/0120150163.

Verdon, J. P., and J. Budge (2018). Examining the capability of statistical models to mitigate induced seismicity during hydraulic fracturing of shale gas reservoirs, *Bull. Seismol. Soc. Am.* **108,** no. 2, 690–701, doi: 10.1785/0120170207.

Verdon, J. P., J. M. Kendall, A. C. Horleston, and A. L. Stork (2016). Subsurface fluid injection and induced seismicity in Southeast Saskatchewan, *Int. J. Greenhouse Gas Control* **54,** Part 2, November 2016, 429–440, doi: 10.1016/j.ijggc.2016.04.007.

Verdon, J. P., J.-M. Kendall, A. L. Stork, R. A. Chadwick, D. J. White, and R. C. Bissell (2013). Comparison of geomechanical deformation induced by megatonne-scale CO_2 storage at Sleipner, Weyburn, and In Salah *Proc. Natl. Acad. Sci. U. S. A.* **110,** no. 30, E2762–E2771, doi: 10.1073/pnas.1302156110.

Viegas, G., A. Baig, W. Coulter, and T. Urbancic (2012). Effective monitoring of reservoir-induced seismicity utilizing integrated surface and downhole seismic networks, *First Break* **30,** no. 7, 77–81.

Walsh, F. R., and M. D. Zoback (2016). Probabilistic assessment of potential fault slip related to injection-induced earthquakes: Application to North-Central Oklahoma, USA, *Geology* **44,** no. 12, 991–994, doi: 10.1130/G38275.1.

Wiseall, A. C., R. J. Cuss, E. Hough, and S. J. Kemp (2018). The role of fault gouge properties on fault reactivation during hydraulic stimulation; an experimental study using analogue faults, *J. Nat. Gas Sci. Eng.* **59,**21–34, doi: 10.1016/j.jngse.2018.08.021.

Manuscript received 14 May 2020
Published online 28 October 2020